ChemComm

REVIEW ARTICLE

View Article Online
View Journal | View Issue

Cite this: *Chem. Commun.*, 2026, **62**, 5832

Stable organic radical luminescent groups and their applications in nano-diagnosis and therapy

Congyan An and Lifeng Yan *

Received 27th December 2025,
Accepted 16th February 2026

DOI: 10.1039/d5cc07360j

rsc.li/chemcomm

The unique singlet-state luminescence mechanism of stable organic radicals avoids the energy loss caused by inter-system crossing in traditional closed-shell molecules, providing a new approach for achieving efficient luminescence. This review focuses on systems such as poly-chlorinated triphenylmethyl derivatives (**PTM**, **TTM**, BTM, *etc.*), di-cyanomethyl radicals, and double radicals. Through strategies such as spatial steric hindrance, electronic delocalization, and structural regulation, their stability and luminescent properties have been significantly improved. In terms of application, organic radical materials demonstrate excellent potential for tumor treatment. Their open shell structure can generate type I reactive oxygen species through an electron transfer mechanism, effectively overcoming the limitations of tumor hypoxic microenvironment on photodynamic therapy. At the same time, their strong near-infrared absorption property enables them to have efficient photothermal conversion ability. The integrated diagnosis and treatment platform constructed through nanotechnology engineering can achieve coordinated treatment under the guidance of near-infrared imaging, providing a new material system for the development of efficient and low-toxic tumor precision treatment strategies.

Introduction

Radical luminescence mechanism

From the perspective of the research object and the number of unpaired electrons, there is an essential difference in the spin state between single radicals and traditional closed-shell molecules. For closed-shell molecules, their ground state is stable, and we study the two unpaired electrons after excitation, one located on the highest occupied molecular orbital in the ground state (HOMO) and the other on the lowest unoccupied molecular orbital in the ground state (LUMO). In the excited state, both orbitals become singly occupied molecular orbitals (SOMOs) When the spins of these two electrons are in the opposite direction, the spin quantum number is 0, corresponding to the singlet state; when they are in same directions, the spin quantum number is 1, which is the triplet state (Fig. 1a). However, for common single radicals, both their ground state and excited state have only one unpaired electron. Therefore, regardless of whether they are excited or not, their

State Key Laboratory of Precision and Intelligent Chemistry, School of Chemistry and Material Science, University of Science and Technology of China, Hefei, Jinzhai Road 96, 230026, Anhui, China. E-mail: lfyan@ustc.edu.cn; Fax: +86-551-63606853; Tel: +86-551-63606853

Congyan An

Congyan An is a second-year master's student in the School of Chemistry and Materials Science at the University of Science and Technology of China (USTC), supervised by Professor Lifeng Yan. She received her bachelor's degree from the School of Materials Science and Engineering at Zhengzhou University in 2024. Her master's research focuses on the application of stable luminescent radicals in near-infrared imaging and tumor theranostics.

Lifeng Yan

Lifeng Yan obtained his PhD degree in Physical Chemistry in 2001 at the University of Science and Technology of China (USTC). He obtained his BSc degree in Chemistry at Zhengzhou University in 1991. He became a full professor in 2012 in the School of Chemistry and Material Sciences, USTC. His main research interests are biomass conversion, degradable polymers for nanomedicine (theranostics), and energy storage.

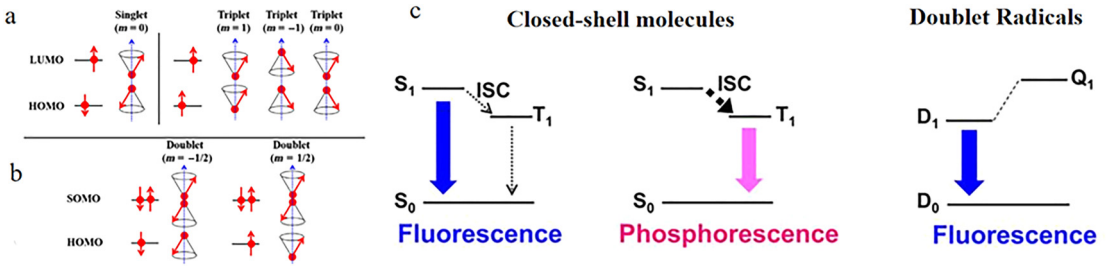

Fig. 1 Schematic diagram of the excited-state spin configurations of a closed-shell molecule (a) and a single radical (b), reproduced from ref. 1 with permission from Chinese Chemical Society, *CCS Chemistry*, 2020, 2, 1129–1145, copyright 2020. (c) Emission dynamics of closed-shell molecules and doublet radicals, reproduced from ref. 2 with permission from American Chemical Society, *Chemical Reviews*, 2024, 124, 1034–1121, copyright 2024. Note: In the excited state, HOMO and LUMO refer to the ground-state orbitals from which the electrons originate.

spin quantum number is always 1/2, and they are all in the doublet state (Fig. 1b).[1]

Traditional closed-shell fluorescent materials are limited by the singlet–triplet energy gap and intersystem crossing processes, which impose a theoretical limit of 25% on their electroluminescent internal quantum efficiency. They follow Hund's first rule, typically having a singlet excited state (S_1, usually emissive) and a lower-energy triplet excited state (T_1, usually non-emissive).[3] The intersystem crossing process from $S_1 \rightarrow T_1$ constitutes the primary fluorescence quenching pathway. Organic radical emitters, due to their unique doublet electronic structure, have a lowest excited state (D_1) and a ground state (D_0) that belong to the same doublet spin manifold, with no dark states of other spin multiplicities in between. This characteristic fundamentally avoids fluorescence quenching caused by intersystem crossing, and the excitons generated by electrical excitation are 100% emissive doublet excitons (Fig. 1c). Therefore, in principle, high fluorescence quantum efficiency can be achieved without relying on technologies such as thermally activated delayed fluorescence or phosphorescence to enhance quantum yield.

Structural design of stable luminescent radicals

The extremely high chemical reactivity and short lifespan of radicals have long been major obstacles to their study and application. Because they contain unpaired electrons, radicals easily trigger non-selective chain reactions, leading to material degradation and biological oxidative damage, and are difficult to store and control. This notion was overturned in 1900 by Gomberg,[4] who unexpectedly discovered that the triphenylmethyl radical could stably exist in solution, proving for the first time that 'persistent radicals' could be obtained through molecular design, thus creating a whole new field of stable radical chemistry.

Researchers have effectively improved the stability of radicals through various molecular design strategies. The core strategies include: using bulky substituents to create steric hindrance, which kinetically shields the reactive centers and can also thermodynamically disfavor dimerization by increasing the free energy of radical–radical coupling processes; achieving electron delocalization through conjugated structures, which thermodynamically disperses the single-electron density; and constructing aromatic backbones or introducing heteroatoms to further stabilize the electronic structure. Steric hindrance can effectively inhibit radical dimerization,[5] and spin delocalization helps reduce the energy gap, thereby lowering the overall energy and reactivity of the radical system.[6] As shown in Fig. 2, thanks to these designs, stable radicals such as TEMPO[7] and DPPH[8] have become indispensable key materials and tools in controlled polymerization, spin labeling, organic batteries, and antioxidants. Stable organic luminescent radicals, as a unique class of functional materials, are increasingly demonstrating broad application potential in areas such as quantum transport,[9] conductive polymers,[10] bio-nano diagnosis and therapy,[11] organic magnets,[12] and catalysis, and therefore are attracting growing attention.

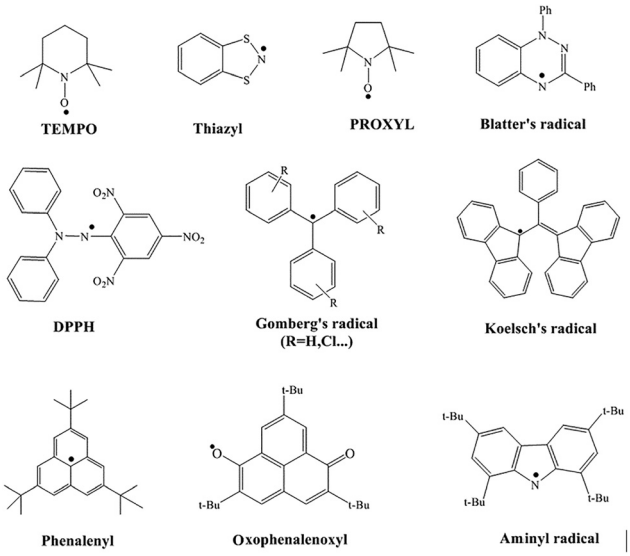

Fig. 2 Some typical stable luminescent radicals.

Stable luminescent radical type

In the early study of luminescent radicals, their practical applications and the in-depth exploration of their photophysical properties faced dual challenges. On one hand, the inherent luminescence quenching effect of radicals severely limited their luminescent performance;[13] on the other hand, their chemical and photochemical instability also brought significant

difficulties for research. Therefore, before the development of polychlorinated triarylmethyl radical systems, progress in this field was relatively limited. Early studies mainly focused on the early 20th century, where researchers often generated unstable radicals *in situ* in frozen solutions[14] and conducted preliminary investigations of their photophysical properties based on this. Currently, with ongoing exploration and research into the structure of luminescent radicals, several types of stable luminescent radicals have been developed. This section primarily introduces several mainstream stable luminescent radicals currently under study and heir photophysical characteristics.

Radicals centered on heteroatoms

Nitrogen and oxygen radicals. Among the many stable organic radicals, nitronyl nitroxide (NN) and imino nitroxide (IN) have become one of the main research directions for stable luminescent radicals since their discovery in the 1970s. In recent years, their luminescent properties have also received widespread attention (Fig. 3). Early studies mainly focused on low-temperature solid-state luminescence. For example, **IMImH** and **NITImH**[15] exhibited emission bands at approximately 573 nm and 683 nm at 5 K, respectively, where **IMImH** showed a mirror relationship between absorption and emission spectra, while **NITImH** displayed non-mirror spectra due to overlapping electronic transitions. Subsequently, it was found that derivatives such as **NN-Pr^{Me}**[16] could also produce solid-state emission in the 750–850 nm range at room temperature, with emission peaks blue-shifting at 77 K and showing vibrational structures with intervals of about 200 cm^{-1}. However, systematic reports on the luminescence quantum yields and lifetimes of simple NN/IN radicals are still lacking. It is worth noting that in 2014, Plyusnin team[17] constructed a molecule **NN-PQ** with dual emission characteristics by combining NN radicals with fluorescent groups (such as 2-pyrazolylquinoline). When excited, this type of material can simultaneously emit

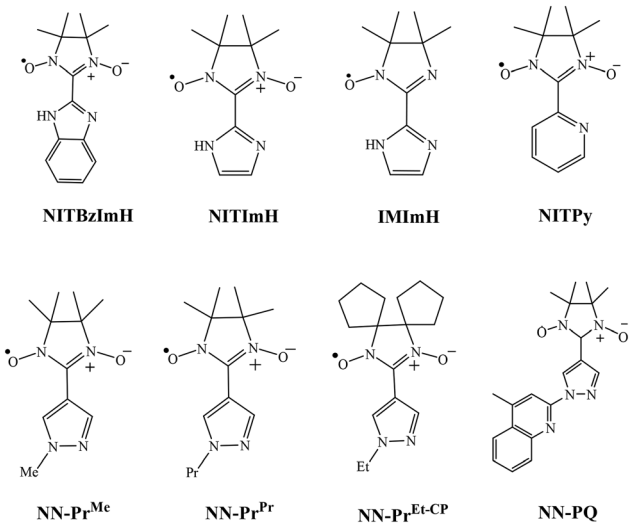

Fig. 3 Some typical nitrogen-oxygen radical.

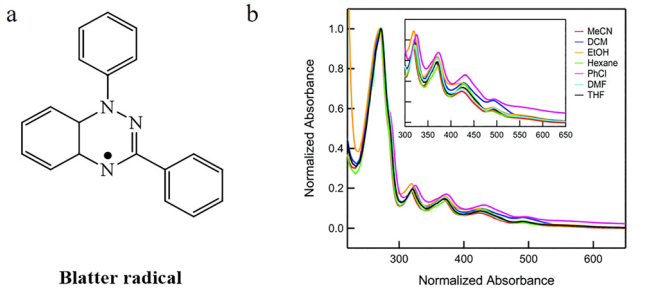

Fig. 4 (a) The structure of Blatter radicals. (b) The absorption of Blatter radical in different solvents. Reproduced from ref. 19 with permission from Royal Society of Chemistry, *New J. Chem.*, 2017, 41, 8604–8613, copyright 2017.

from the fluorescent groups (around 390–425 nm) and from the local orbital transitions of the radical (around 692–745 nm) in either room temperature solutions or solid states, but their quantum yields are generally low, which may be due to energy transfer from the fluorescent groups to the radicals.

Blatter radical. Blatter radicals[18] (Fig. 4a), as a class of stable organic radicals first reported as early as 1968, had their luminescent properties systematically studied only in 2017 by Hayes *et al.*[19] This study revealed, that these radicals exhibit multi-band absorption characteristics in solution (Fig. 4b), with emission spectra covering the long-wavelength region of 600–700 nm. This emission is believed to mainly originate from NLUMO → SOMO electronic transitions and shows significant dependence on solvent, concentration, and excitation wavelength. Notably, under 370 nm excitation in different solvent (Fig. 4c), these radicals can produce broadband emission covering 400–700 nm, displaying white-light emission characteristics.

In subsequent research, scientists have prepared a series of Blatter radical derivatives through strategies such as planarization,[20] fluorination,[21] and heterocycle fusion,[22] achieving systematic modulation of the structure and photoelectronic properties of the Blatter radical. These derivatives exhibit broad absorption across the visible to near-infrared region, tunable band gaps, and unique magnetic exchange behavior. However, as the corresponding literature does not mention fluorescence emission behavior in these Blatter radical derivatives, it will not be further elaborated in this section.

Carbon radicals

Polychlorotriphenylmethyl radical. Polychlorinated triarylmethyl (TArM) radicals have become one of the most prominent systems among luminescent radicals due to their excellent chemical stability, unique photoluminescent properties at room temperature, and ease of structural modification. Numerous radicals of this type have already been successfully synthesized and characterized. Current research mainly focuses on their fundamental luminescent properties, theoretical explanations of their luminescent mechanisms, and breakthroughs in luminescent functionality. As shown in Fig. 5, this section will describe the luminescent characteristics of several classic TArM examples, highlighting the developmental history of this field.

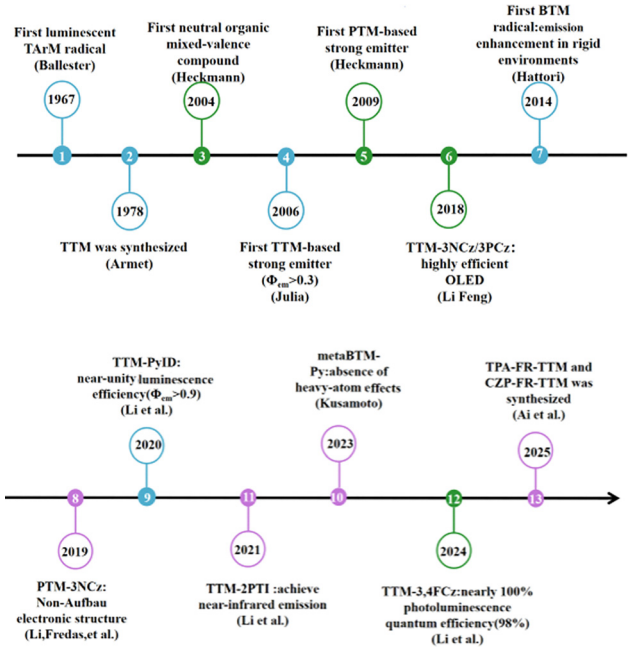

Fig. 5 Development of polychlorinated triphenylmethyl radicals.

Perchlorotriphenylmethyl radical (PTM). **PTM** is the first reported polychlorinated triphenylmethyl radical, synthesized by Ballester in 1967.[23] Its stability arises from its unique spatial and electronic structure (as shown in Fig. 6): the three fully chlorinated phenyl rings are arranged in a propeller shape, and the ortho chlorines shield the central carbon atom through steric hindrance, achieving kinetic stability; meanwhile, the sp^2 hybridization of the central carbon allows spin delocalization onto the phenyl rings, providing thermodynamic stability. Therefore, **PTM** can remain stable both in the solid state and in dilute solution. The luminescent properties of **PTM** were first reported by the Fox team[24,25] in 1987. The report indicated that **PTM** appears bright red in CCl_4, with its absorption spectrum extending beyond 600 nm, suggesting strong absorption in the visible region. The maximum emission wavelength is at 606 nm, and its fluorescence quantum yield depends on the excitation wavelength; when excited at 530 nm, ϕ_{em} = 0.015. Its fluorescence lifetime τ = 7 ns, which is relatively short, indicating the presence of efficient non-radiative or chemical processes. This section focuses on the derivatives of **PTM** radicals, discussing their optical properties. The optical characteristics of the mentioned molecules have been compiled in Table 1.

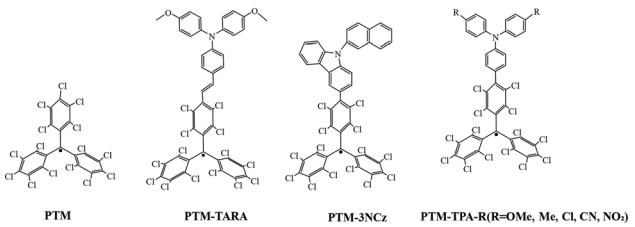

Fig. 6 Typical **PTM** radicals mentioned in the text.

Table 1 Photophysical characteristics of **PTM** radicals

Radical	λ_{abs} (nm)	λ_{em} (nm)	Φ_{em} (%)	Solvent
PTM	375	605	1.5/377	CCl_4
PTM-3NCz	380, 607	680	54.0/380 52.0/607	Cyclohexane
PTM-TARA	12 300	—	—	*n*-Hexane
PTM-TPA-OMe	12 700	11 300	4/384 3/760	Cyclohexane
PTM-TPA-Me	13 150	11 810	15/384 15/700	Cyclohexane
PTM-TPA-Cl	15 500	13 100	14/380 3/564	Cyclohexane
PTM-TPA-NO_2	—	14 350	11/380 35/564	Cyclohexane
PTM-TPA-CN	—	14 750	—	Cyclohexane

In 2004, Heckmann[26] successfully introduced triarylamine (TARA) moiety into **PTM** structures, thereby preparing neutral organic mixed-valence (MV) compounds for the first time (Fig. 6 **PTM-TARA**). In 2009,[27] the team further synthesized a series of PTM-TPA radical derivatives, which exhibited strong charge transfer (CT) absorption bands in the visible to near-infrared region (approximately 12 500–18 000 cm^{-1}), accompanied by rare strong near-infrared fluorescence emission. Substituents on the TARA part (such as OMe, Me, Cl, CN, NO_2) can adjust the donor strength, thus systematically regulating the CT state energy. The stronger the donor, the more pronounced the redshift in CT absorption and emission. Compared to unsubstituted **PTM** ($\Phi_f \approx 0.015$), the fluorescence quantum yield of TPA-PTM derivatives can increase up to 150 times, reaching a maximum of $\Phi_f \approx 0.40$. These characteristics make the TPA-PTM system not only valuable for fundamental photophysical research but also provide new ideas for developing near-infrared fluorescent materials, molecular electronic devices, and light energy conversion systems.

In recent years, researchers have discovered new findings in the synthesis of **PTM** derivatives: introducing substituents with strong electron-donating ability to **PTM** may violate the Aufbau principle.[28] Researchers covalently combined electron-deficient fully chlorinated triphenylmethyl (**PTM**) with electron-rich donors (such as carbazole derivatives) to form donor–acceptor type neutral radicals (D–A$^{\bullet}$). In this work, the **PTM-3NCz**, designed as a donor–acceptor-based non-Aufbau radical, exhibits a singly occupied molecular orbital (SOMO, localized on the radical unit) lying below the doubly occupied highest occupied molecular orbital (HOMO, localized on the donor unit), forming a SOMO–HOMO inversion (Fig. 7b). This structural feature leads to significantly improved key performance metrics compared to the conventional **PTM** radical. By comparing the absorption and fluorescence spectra of **PTM** and **PTM-3NCz** in cyclohexane, the fluorescence peak of **PTM-3NCz** shows a notable redshift to approximately 680 nm (Fig. 7a), accompanied by a substantial enhancement in fluorescence intensity. The fluorescence quantum yield increases from 1.6% to 54% (Table 1), demonstrating superior photostability. As shown in Fig. 7c and d, under pulsed laser irradiation at 355 nm, the fluorescence intensity half-life of **PTM-3NCz**

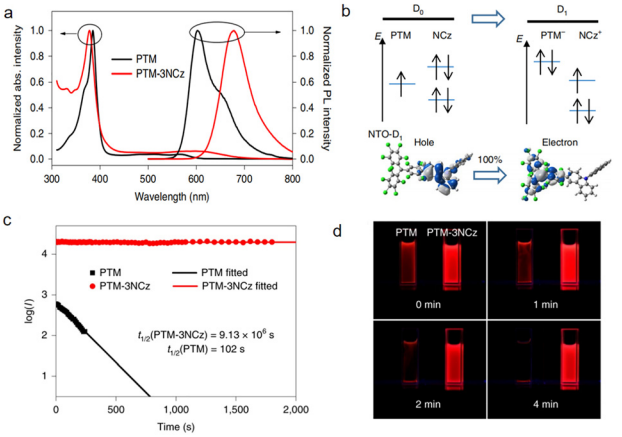

Fig. 7 Photophysical properties and photostability of the **PTM-3NCz** radical. (a) Optical absorption and fluorescence spectra of the **PTM** and **PTM-3NCz** radicals in cyclohexane. (b) Schematics of the electronic transition process between the ground state (D_0) and the first excited state (D_1) in **PTM-3NCz**. (c) Time dependence of the emission intensities (I) of the **PTM** and **PTM-3NCz** radicals in dilute cyclohexane under 355-nm laser radiation. (d) Photographs of **PTM** and **PTM-3NCz** in dilute cyclohexane solution under a 365-nm ultraviolet lamp as a function of time. reproduced from ref. 28 with permission from Springer Nature, *Nature Materials*, 2019, 18, 977–984, copyright 2019.

reaches about 10^6 seconds (Fig. 7c), which is nearly five orders of magnitude longer than that of the conventional **PTM** radical.

Tris(2,4,6-trichlorophenyl)methyl radicals (TTM)

TTM radicals also belong to the category of polychlorinated aryl radicals and are currently the most extensively studied stable luminescent radicals. In 1978, Armet[29] first synthesized the **TTM** radical (Fig. 8) using 1,3,5-trichlorobenzene and chloroform as raw materials through a Friedel–Crafts reaction followed by a dehydrogenation oxidation reaction. This general synthetic method is still in use today. The structure of **TTM** is very similar to **PTM**, except that each benzene ring contains three non-adjacent chlorine atoms. The sp^2 hybridization of the central carbon atom facilitates spin delocalization, the six internal chlorine atoms provide steric shielding, and the three

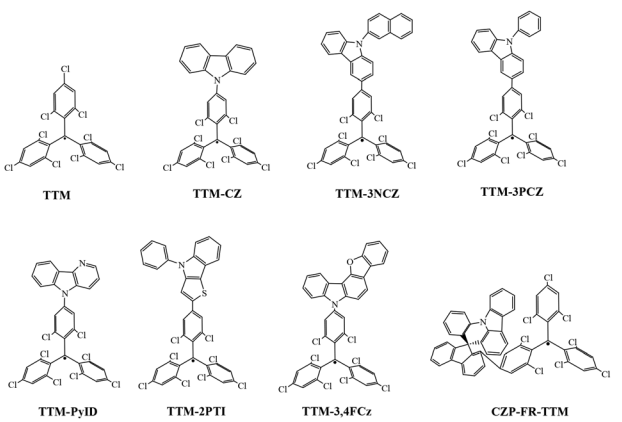

Fig. 8 Typical **TTM** radicals mentioned in the text.

Table 2 Photophysical characteristics of **TTM** radicals

Radical	λ_{abs} (nm)	λ_{em} (nm)	Φ_{em} (%)	Solvent
TTM	373, 542	570	2	CH_2Cl_2
TTM-Cz	603	628	53	Cyclohexane
TTM-3NCz	375, 616	708	49	Toluene
TTM-3PCz	375, 624	695	46	Toluene
TTM-PyID	—	643	99	$CHCl_3$
TTM-2PTI	376, 707	830	1	Toluene
TTM-3,4FCz	375, 611	657	98	Cyclohexane
CZP-FR-TTM	375, 550	634	64.3	Cyclohexane

external chlorine atoms prevent dimer formation. These factors collectively endow **TTM** with excellent chemical stability. However, its photostability is relatively poor; under 370 nm light irradiation, the decay time of the photoluminescence in different solvents is about 200 seconds, with a relatively short half-life. In 2006, this issue was successfully addressed by Julia's team,[30] who attached carbazole groups to **TTM** to synthesize **TTM-Cz**, enhancing the photostability of the radical and significantly prolonging its half-life. Furthermore, the molecule exhibits excellent red luminescent properties, with a fluorescence quantum yield as high as 53% in cyclohexane. This section focuses on the derivatives of **TTM** radicals, discussing their optical properties. The optical characteristics of the mentioned molecules have been compiled in Table 2.

In 2015, Li group[31] first proposed and verified a novel strategy of using the neutral π-radical **TTM-Cz** as the emissive layer to construct organic light-emitting diodes (OLEDs) with doublet emission characteristics. The unique electronic structure of this molecule lies in its highest occupied orbital being a singly occupied molecular orbital (SOMO). Theoretical calculations and spectral analysis indicate (Fig. 9a and b) that both its photoluminescence and electroluminescence originate from the transition of an electron from the lowest unoccupied molecular orbital (SUMO) to the SOMO. Since both the ground state and the excited state involve only a single unpaired electron, the excited state is a doublet, and its radiative decay is fully spin-allowed, theoretically enabling the device IQE to reach 100%. Solution-processed doped OLEDs based on **TTM-1Cz** achieved deep red/near-infrared emission (peak around 660 nm) (Fig. 9b), with a maximum external quantum efficiency of 2.4%, which was comparable among OLEDs (Fig. 9c) of similar wavelengths at that time. Moreover, in 2018, this research group synthesized two novel luminescent radicals, **TTM-3NCz** and **TTM-3PCz**[32] (Fig. 8). By covalently attaching carbazole-derived donors to the **TTM** radical acceptors, they constructed a D_1 excited state with significant charge transfer characteristics, achieving a photoluminescence quantum yield of up to 85.6% in solid-state films. At the device level, OLEDs based on **TTM-3NCz** reached a maximum external quantum efficiency of 27% in the deep red/near-infrared region (710 nm), setting a record for LED efficiency in this wavelength range. This efficiency not only far exceeds the theoretical limit of conventional fluorescent materials but also significantly outperforms other contemporary technical approaches.

In 2020, this group systematically elucidated the luminescence mechanism of organic radicals and established universal

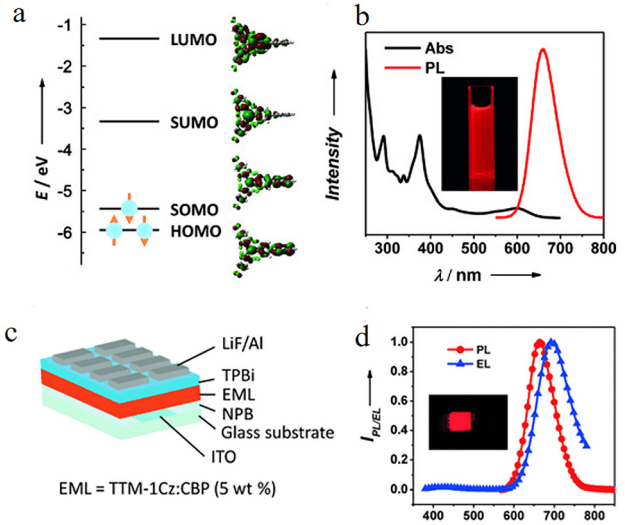

Fig. 9 (a) The energy levels (left panels) and contour plots (right panels) of the molecular orbitals (LUMO, SUMO, SOMO, and HOMO) of **TTM-1Cz**. (b) The UV/Vis Abs and PL spectra of **TTM-1Cz** in chloroform solution. (c) The schematic diagram of the structure of **TTM-1Cz** based OLEDs. (d) The EL spectrum (7 V) of the OLEDs accompanied by the PL spectra of the doped thin film. reproduced from ref. 31 with permission from Wiley, *Angew. Chem., Int. Ed.*, 2015, 54, 7091–7095, copyright 2015.

molecular design guidelines.[33] For the first time, the study revealed from a quantum mechanical perspective that the fundamental reason for the low luminescence efficiency of conventional **TTM** and other alternating hydrocarbon radicals is the degenerate HOMO–SOMO and SOMO–LUMO gaps, leading to the lowest excited state (D_1) being composed of two out-of-phase degenerate transitions, with an almost zero oscillator strength. Based on this, the researchers proposed two groundbreaking design principles: (1) non-alternating hydrocarbon systems must be constructed to break the degeneracy; (2) chemical bonding should be used to allow the D_1 state with charge transfer (CT) characteristics to 'borrow intensity' from the high-energy bright state (D_2) of the radical unit, thereby significantly enhancing its radiative transition probability. This provides a new theoretical framework for understanding and designing luminescent radicals. Utilizing these guidelines, the researchers successfully designed TTM-pyridine-indole derivatives, achieving high-efficiency pure red emission with photoluminescence quantum yields above 90%, and fabricated OLEDs with external quantum efficiencies exceeding 12%. This work marks a transition in the field from empirical exploration to rational design.

In recent years, research on organic luminescent radicals centered on **TTM** has achieved a series of significant advances in extending emission wavelengths, and improving luminescence efficiency and stability. In 2023, Li[34] designed and synthesized **TTM-2PTI** (Fig. 8) by introducing a thieno[3,2-*b*]-indole group to replace the conventional carbazole. By leveraging its lower steric hindrance and stronger electron-donating ability, they successfully red-shifted the emission peaks to 830 nm in solution and 870 nm in devices, achieving the longest electroluminescence wavelength for dual-state near-infrared OLEDs at that time. In 2024, the team further improved the PLQE of the carbazole 3,4-ring-fused derivative **TTM-3,4FCz**[35] to nearly the theoretical limit of 98.0% by precisely adjusting the effective distance between donor and acceptor (D–A) within the conventional through-bond charge transfer (TBCT) framework, revealing the decisive role of structural fine-tuning in balancing radiative and non-radiative processes. In 2025, Ai and her colleagues[36] shifted their focus to mechanistic innovation, successfully constructing the first **TTM** radicals emitting *via* the through-space charge transfer (TSCT) mechanism (such as TPA-FR-TTM in Fig. 8). By using a rigid fluorenyl linker to achieve spatial proximity and non-bonded interaction between the donor and radical units, this design not only significantly weakened electron-vibration coupling, reducing the non-radiative decay rate to an ultra-low level, but also induced the formation of non-Aufbau electronic structures, greatly enhancing the photochemical and thermal stability of the radicals.

Pyridyl-substituted bis(trichlorophenyl)methyl radical (BTM)

In 2014, Hattori[37] cleverly replaced one of the phenyl rings in the **TTM** radical with a para-substituted pyridine, forming the **PyBTM** radical (Fig. 10). Although its molecular framework is very similar to that of **TTM**, its physical and chemical properties differ significantly. The most direct manifestation is its enhanced stability. Although the PLQE of **PyBTM** in dichloromethane at room temperature is only 2%, it can reach 81% in EPA solvent at low temperature (77 K). This section focuses on the derivatives of BTM radicals, discussing their optical properties. The optical characteristics of the mentioned molecules have been compiled in Table 3.

In 2015, Hattori[38] also synthesized **PyBTM** radicals with different halogen substitutions and studied them (Fig. 10). As F/Cl/Br were varied, the fluorescence emission of the radicals changed from yellow to orange and then to red (Fig. 11), and their photostability also improved.

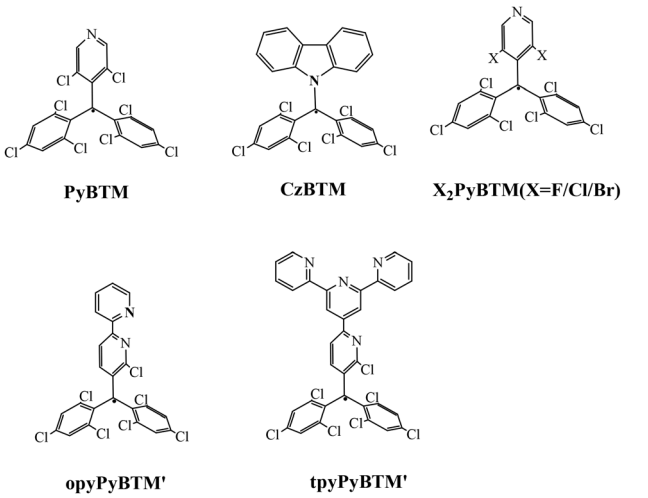

Fig. 10 Typical BTM radicals mentioned in the text.

Table 3 Photophysical characteristics of **PTM** radicals

Radical	λ_{abs} (nm)	λ_{em} (nm)	Φ_{em} (%)	Solvent
PyBTM	370, 541	585	3	CH_2Cl_2
CzBTM	284, 387, 514, 554	697	2	Cyclohexane
F_2PyBTM	351, 523	566	4	CH_2Cl_2
Cl_2PyBTM	370, 541	585	2	CH_2Cl_2
Br_2PyBTM	376, 548	593	2	CH_2Cl_2

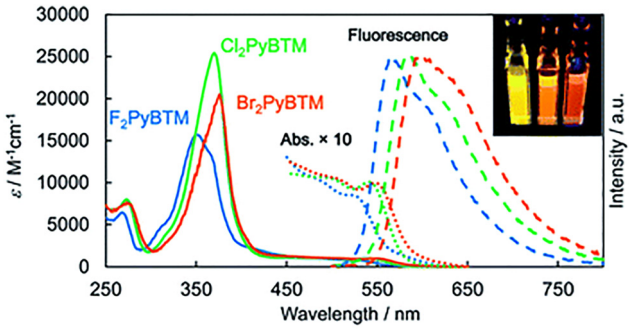

Fig. 11 Absorption (solid lines) and corrected emission spectra (dashed lines) of **Br_2PyBTM**, **Cl_2PyBTM**, and **F_2PyBTM** in CH_2Cl_2, reproduced from ref. 38 with permission from Royal Society of Chemistry, *RSC Adv.*, 2015, 5, 64802–64805, copyright 2015.

In 2018, a new radical molecule, **CzBTM**[39] (Fig. 10), was successfully synthesized by Ai's team. **CzBTM** exhibits deep red to NIR emission spectra in various solvents, but its PLQE (2% in cyclohexane) is relatively low. In the same year, Harrori's team synthesized two novel radicals, **oPyPyBTM′** and **tpyPyBTM′**,[40] and by introducing pyridine or terpyridine groups into the molecules, they significantly enhanced their coordination ability with protons and metal ions. The key finding was that the fluorescence quantum yield of these radicals was significantly increased upon binding with H^+ or Zn^{2+}, achieving a 'turn-on' type fluorescence response. A more important theoretical contribution of this work was the first proposal and experimental verification that radical emission is insensitive to internal and external heavy atom effects. For conventional closed-shell fluorescent molecules, heavy atoms (such as iodine or lanthanide ions) can promote intersystem crossing (ISC) through enhanced spin–orbit coupling, leading to fluorescence quenching. However, radical emission originates from allowed doublet-to-doublet ($D_1 \rightarrow D_0$) transitions and does not involve the ISC process. Experiments confirmed that even under conditions with ethyl iodide (external heavy atom effect) or coordination with La^{3+} (internal heavy atom effect), the non-radiative decay rate (k_{nr}) of the radicals did not significantly increase, allowing the fluorescence to be retained. This indicates that radical emission may offer unique stability and reliability advantages over conventional fluorophores in complex chemical environments or biosensing applications.

Dicyanomethyl radical

Early studies revealed that the dicyanomethyl radical was not found to be stable as a monomer in the presence of a benzene ring. In 1966, Hartzler first[41] accounted for this instability, as

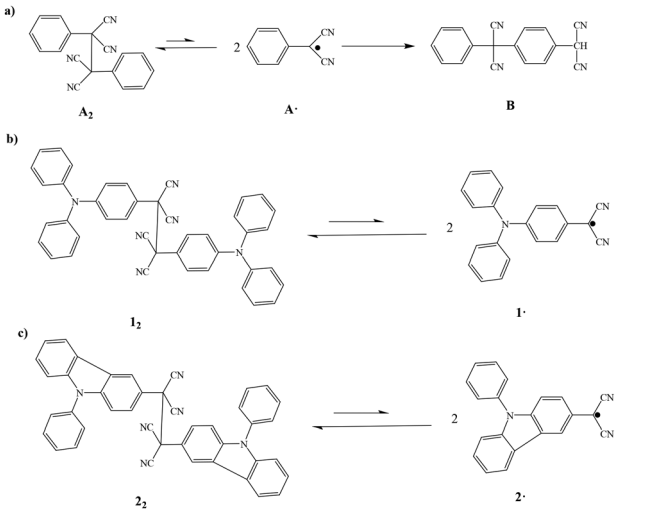

Fig. 12 (a) Equilibrium between A_2 and A•, and isomerization to B. (b) Equilibrium between 1_2 and 1•, (c) equilibrium between 2_2 and 2•, reproduced from ref. 45 with permission from Wiley, *Angew. Chem., Int. Ed.*, 2016, 55, 8634-8638, copyright 2016.

illustrated in Fig. 12a, 1,2-diphenyl-1,1,2,2-tetracyanoethane (A_2), which is regarded as the dimer of the phenyldicyanomethyl radical (A•), is in equilibrium with A• in solution. Because the hydrogen on the para position of the benzene ring linked to the cyano methyl radical is very reactive, two A• radicals easily combine to form a B molecule.

To obtain the dicyanomethyl radical in a stable, monomeric state. It has been reported that introducing substituents such as methyl, chlorine, or nitro groups at the para position of the dicyanomethyl group can inhibit such isomerization reactions.[42–44] In 2016, Kobashi *et al.*[45] chose triphenylamine (Fig. 12b) and carbazole (Fig. 12c) as the framework and introduced dicyanomethyl radicals onto them. The ingenious aspect of this design is that the strong electron-donating properties of the framework not only effectively stabilize the radical form through spin delocalization but also prevent the irreversible side reactions that similar radicals (such as the system reported by Hartzler in 1966) are prone to, thereby obtaining ideal monomers with both high stability and moderate dynamic behavior. In 2017, J.P. Peterson team[46] systematically and quantitatively revealed the regulatory rules of substituent effects on the strength of their dynamic covalent bonds. It was unambiguously demonstrated that the push–pull effect—where electron-donating groups significantly weaken bonding by stabilizing the radical state, while electron-withdrawing groups strengthen it—plays a key role.

In the same year, Okino[47] revealed that the dimerization behavior of amino-substituted dicyanomethyl radicals can be fundamentally switched through fine-tuning of the electron-donating structure, and for the first time, they thoroughly elucidated the role of electrostatic interactions as a key driving force in the π-dimerization of neutral radicals. Among them, DT• and PT• (Fig. 13a and b) exhibit behavior similar to known systems, existing in dynamic equilibrium with σ-dimers connected

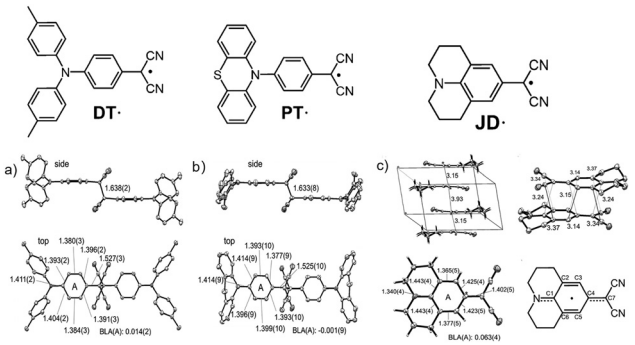

Fig. 13 X-ray crystal structures of (a) **DT•** and (b) **PT•** and (c) **JD•**, reproduced from ref. 47 with permission from Wiley, Angew. Chem., Int. Ed., 2017, 56, 16597–16601, copyright 2017.

by long C–C bonds (1.63 Å) both in solution and solid state, and are considered "dynamically stabilized" radicals. JD•, however, shows completely unique behavior: it does not form σ-dimers and can be isolated as a "stable" radical without bulky protecting groups; X-ray single-crystal analysis shows that in the solid state, it forms π-dimers *via* face-to-face stacking (Fig. 13c); and variable-temperature spectroscopy confirms that it also exists in equilibrium with π-dimers in toluene solution.

In 2021, Zhang[48] proposed a novel electronic strategy for stabilizing radicals: using the radical center as an "electron pool" to achieve electronic stabilization of the radical by alleviating the anti-aromaticity of the connected groups. The authors synthesized constrained coplanarity between strong substituents and the radical center by introducing bridged rings (molecule 4,5,7,8 in Fig. 14a), successfully achieving strong mixing of electronic states. When rings with anti-aromaticity (such as phenoxazine) are forced to remain coplanar with the radical center through synthetic bridges, the radical spin can delocalize onto the substituents, greatly enhancing the monomer stability. Experiments confirmed that radicals with such conformationally constrained anti-aromatic substituents have dimerization equilibrium constants (Fig. 14b) more than six orders of magnitude lower than radicals with aromatic substituents, directly demonstrating the counterintuitive rule that "the stronger the anti-aromaticity, the more stable the radical". As shown in Fig. 14c, the most stable radical 8 formed an unprecedented *ortho–ortho* ring σ-dimer in the solid state, rather than the commonly observed head-to-head σ-dimer. Computational analysis suggested that this may be due to spin delocalization reducing the tendency for head-to-head dimerization, while London dispersion forces play a key stabilizing role in this unique stacking pattern. This approach breaks through the traditional stabilization methods that rely on steric hindrance or simple conjugation extension, opening a new route for the rational design of electronically stabilized radical materials.

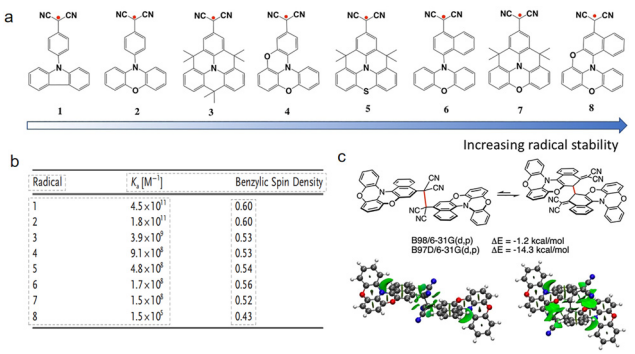

Fig. 14 (a) Anti-aromatic free radicals, ordered by stability as measured by K_a values. (b) K_a values and (c) (Top) computed relative electronic energies (gas) for the two Sigma dimers of 8 with the same functional; the same functional, but one including a dispersion correction; (Bottom) non-covalent interactions plot showing dispersion interactions, reproduced from ref. 48 with permission from the Wiley, *Angew. Chem., Int. Ed.*, 2021, 60, 25082–25088, copyright 2021.

In recent years, researchers have begun to study the luminescent behavior of these radicals. In 2019, this team introduced sulfur/oxygen atoms into the triphenylamine framework to fix the coplanarity of the amino group and the benzene ring, designing and synthesizing a new class of dicyanomethyl radicals (SDP•, ODP•, O2DP•)[49] as shown in the Fig. 15. This caused an unprecedented drastic red shift in the characteristic absorption bands of the radicals (Fig. 15), shifting from 712 nm for the previously reported analogous DP• to 1050 nm, 934 nm, and 1059 nm, respectively, for the new radicals, marking the first time that the main absorption peak of such radicals was extended into the near-infrared region. This achieved a significant red shift of their absorption spectrum from the visible light region (700 nm) to the near-infrared region (up to 1059 nm). Among them, the doubly oxygen-bridged O2DP• is particularly notable; it maintains high transparency and nearly

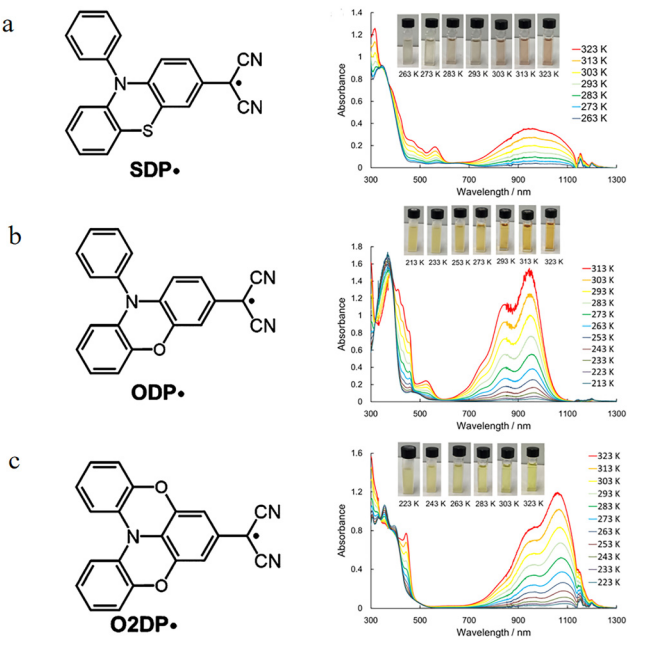

Fig. 15 Molecular structure and corresponding ultraviolet absorption spectra of (a) **SDP•** and (b) **ODP•** and (c) **O2DP•**, reproduced from ref. 49 with permission from American Chemical Society, *ACS Materials Letters*, 2019, 1, 25–29, copyright 2019.

unchanged color in the visible region across the entire temperature range, while its near-infrared absorption intensity undergoes drastic and reversible changes with temperature, exhibiting a unique 'visible-light transparent–near-infrared thermochromic' behavior.

In 2025, our team[50] successfully designed a novel and stable dicyanomethyl radical derivative, CNPJ (as shown in the Fig. 16a), and successfully applied it to near-infrared II fluorescence imaging-guided mild photothermal therapy. By precisely introducing electron-donating julolidine groups into the dicyanomethyl-functionalized phenoxazine scaffold, CNPJ was endowed with a unique property: polarity-dependent radical center migration. In polar solvents, through effective spin delocalization and intermolecular charge transfer, the radical center can migrate from the carbon atom to the nitrogen atom of the julolidine, a phenomenon confirmed by variable-temperature EPR and theoretical calculations (as shown in the Fig. 16b and c). Unlike the reported σ-dimers, CNPJ in solution (toluene) exhibits a temperature-dependent reversible equilibrium between monomers and π-dimers. Variable-temperature UV-vis spectroscopy in the near-infrared region observed characteristic absorption bands attributed to π-dimers (894–1031 nm), with the absorption increasing as the temperature decreases. This π-dimerization and head-to-tail stacking mode enhances molecular rigidity. Benefiting from the increased structural rigidity and π-dimer formation, after nanoassembly, CNPJ exhibits an absolute fluorescence quantum yield of up to 2.57% in the near-infrared II region (NIR-II, 1000–1700 nm), which is an exceptionally high value for low-molecular-weight NIR-II emitters, laying the foundation for ultra-bright *in vivo* imaging. This work marks an important breakthrough in advancing this type of radical from fundamental materials research to biomedical applications.

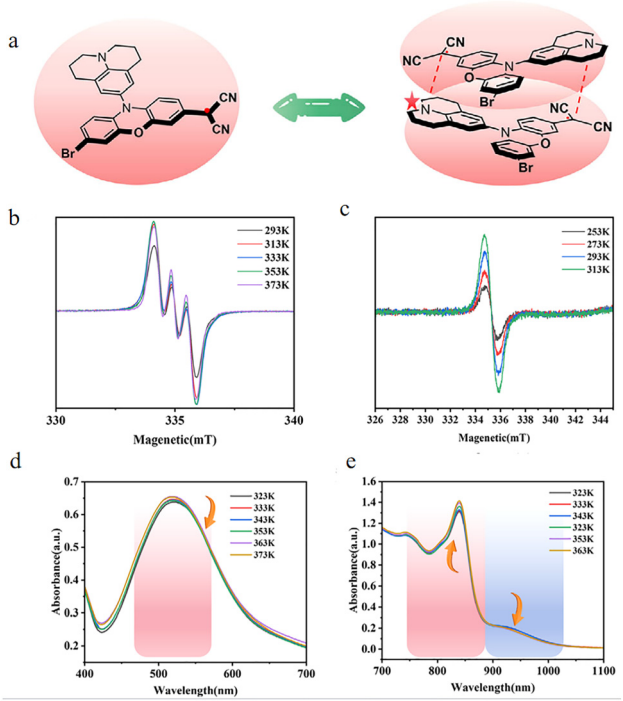

Fig. 16 (a) CNPJ and its dimer. Variable-temperature EPR spectra of (b) CNPJ in DMF and (c) CNPJ in toluene. Variable-temperature UV–vis spectra of CNPJ at (d) 400–700 nm and (e) 700–1100 nm in toluene, reproduced from ref. 50 with permission from Wiley, Angew. Chem., Int. Ed., 2025, 64, e202509609, copyright 2025.

Diradical

Luminescent diradicals, as a class of open-shell molecules with two unpaired electrons, exhibit high sensitivity in their photophysical properties to external stimuli such as temperature, magnetic fields, and microwaves.[51] This sensitivity allows their spin states and luminescent behavior to be effectively controlled, distinguishing them significantly from conventional closed-shell luminescent molecules and single-radical luminescent systems. Based on these characteristics, luminescent diradicals show broad application prospects in conductive materials,[52] optoelectronic materials,[53] spintronics, and quantum information technologies. Since 2023, the field has developed rapidly, with many stable luminescent diradicals and their applications being actively explored. This section focuses on the recent progress and breakthroughs in stable luminescent diradicals, explaining the types of diradicals and their luminescent properties. Delocalized luminescent diradicals are more stable than localized ones and can be classified as Kekulé or non-Kekulé types, depending on whether there is resonance between the closed-shell and open-shell forms.

Since 2023, this field has developed rapidly, and numerous stable luminescent diradicals and their applications are being actively explored. This section focuses on recent progress and breakthroughs in stable luminescent diradicals, explaining their types and luminescent properties. Delocalized luminescent diradicals have higher stability than localized diradicals and can be classified as Kekulé-type or non-Kekulé-type,[54] depending on whether resonance exists between the closed-shell and open-shell forms (Fig. 17).

Kekulé-type luminescent diradicals

Kekulé-type diradicals are based on the classic carbon-hydrogen diradical systems, such as Thiele hydrocarbons, Chichibabin hydrocarbons, and Müller hydrocarbons.[55] These molecules

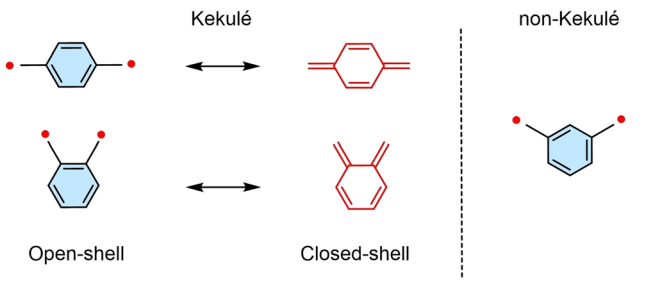

Fig. 17 Representative structure of delocalized diradicals, reproduced from ref. 54 with permission from Wiley, *Angew. Chem., Int. Ed.*, 2025, 64, e202423470, copyright 2025.

exhibit resonance between open-shell and closed-shell forms, forming so-called 'resonance hybrid' structures, which inherently give them diradical characteristics.[56] However, traditional Kekulé hydrocarbons are often limited in practical applications due to their high reactivity and synthetic difficulty.

In recent years, by introducing stabilizing groups, especially tris(2,4,6-trichlorophenyl)methyl (**TTM**) and its analogs, successful functionalization and stabilization of these diradicals have been achieved. Fig. 18 illustrates several Kekulé-type radicals that have been discovered through research in recent years. For example, **TTM-PhTTM**,[57] as the first stable luminescent Müller hydrocarbon derivative, features a structure in which two **TTM** units are connected *via* a phenyl bridge. The molecule exhibits approximately 90% diradical character, with a small singlet–triplet energy gap ($\Delta E_{S-T} \approx 1.51$ kcal mol^{-1}) and emits in the deep red region (671 nm). However, its luminescence quantum yield is relatively low (0.4%), which limits its further applications. In 2024, Uchida and co-workers synthesized PyBTM-(Hex$_2$Ph)PyBTM[58] by introducing alkyl substituents on the bridging phenyl ring. Through twisted conjugation that suppresses non-radiative transitions, this molecule successfully increased luminescence efficiency to 12% (in PMMA films), highlighting the crucial role of molecular design in enhancing luminescent performance.

Apart from the Müller hydrocarbon system, Chichibabin-type diradicals such as SDs[59] and **TTM–TTM**,[60] as well as Thiele-type diradicals like TFCs[61] and TTH,[62] have also been reported. Among them, TFCs exhibit nearly 100% luminescence quantum yield in solution, with their emission originating from a quenchable zwitterionic excited state formed after photoexcitation, showcasing the unique 'sudden polarization' phenomenon in diradical systems. In addition, by extending π-conjugation, such as introducing a cyclopentadithiophene-bridged (M$_3$TTM)$_2$CDT,[63] or enhancing intramolecular push–pull electronic effects, such as PhNVDPP and 2PhNVDPP,[64] the absorption and emission wavelengths can be further tuned to the near-infrared II region, expanding their potential applications in bioimaging and photothermal therapy.

Non-Kekulé-type luminescent diradicals

Non-Kekulé luminescent diradicals, as a unique class of molecules in organic radical chemistry, have attracted widespread attention in recent years. Unlike Kekulé diradicals, non-Kekulé molecules possess a fully conjugated π system, but in their Kekulé structure, at least two atoms do not participate in π bonding.[65] This structural feature endows them with unique electronic structures and photophysical behaviors. As shown in Fig. 19, recently reported non-Kekulé diradicals mainly include the **TTM** type and metaPyBTM typedemonstrating significant advantages in luminescence efficiency, stability, and functional tunability.

TTM-type molecules use tris(2,4,6-trichlorophenyl)methyl (**TTM**) as the radical center, constructing diradical systems through conjugated bridges or spatial coupling. For example, the **DRI** molecules designed by Abdurahman *et al.*[66] achieved a photoluminescence quantum yield (PLQY) of up to 16% by adjusting the conjugation degree of the donor. Their emission wavelength red-shifts with solvent polarity, indicating that the excited state has charge-transfer characteristics. Further incorporation of such diradicals into the polymer backbone yields PDI,[67] which achieves a PLQY of 44% in the solid state, significantly improving material stability and practicality, and has been successfully used in deep-red OLED devices.

In pyridine-based **TTM**-type (metaPyBTM-type) diradicals, the Lambert team[68] in 2019 synthesized a series of TPA- and TPB-bridged **PyBTM** diradicals using triphenylamine and tri(2,6-dimethylphenyl)borane as bridges. These molecules exhibited significant intramolecular charge transfer characteristics, with the lowest-energy absorption attributed to charge transfer from the bridging units to the **PyBTM** radical, providing an example for tuning the emission color of diradicals. In 2023, the Kusamoto team[69] innovatively employed a spatial proximity strategy to design THDBA-2PyBTM, featuring 5,6,8,9-tetrahydro-7-phenyl-dibenz[*c*,*h*]acridine as a rigid bridge. In this molecule, the two **PyBTM** units are arranged in parallel and interact weakly through space, allowing, for the first time, the observation of double emission from both radical pairs and

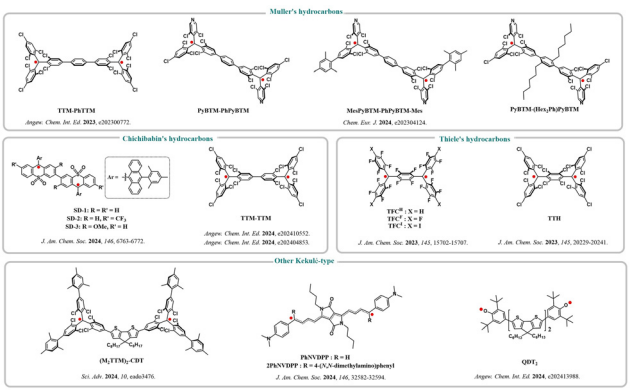

Fig. 18 Chemical structures of Kekulé-type luminescent diradicals, reproduced from ref. 54 with permission from Wiley, *Angew. Chem., Int. Ed.*, 2025, 64, e202423470, copyright 2025.

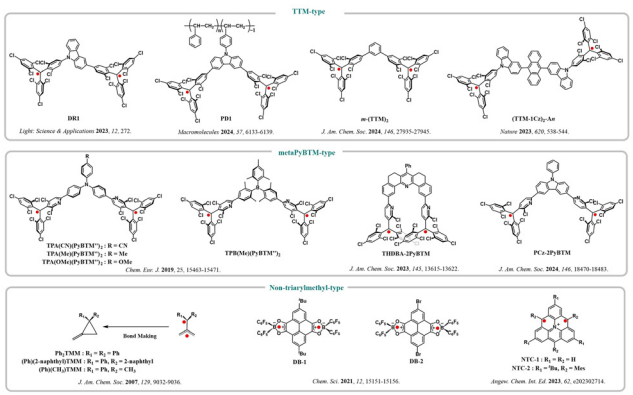

Fig. 19 Chemical structures of non-Kekulé-type luminescent diradicals, reproduced from ref. 54 with permission from Wiley, *Angew. Chem., Int. Ed.*, 2025, 64, e202423470, copyright 2025.

quasi-excimers in a single-molecule diradical system, revealing that the emission intensity can be reversibly modulated by an external magnetic field, achieving a pioneering single-molecule magnetically induced luminescence.

To further explore the relationship between spin coupling and luminescence, the Kusamoto team[70] in 2024 synthesized a symmetric diradical, PCz-2PyBTM, using carbazole as a conjugated bridge. This molecule exhibited strong solvent-dependent fluorescence color changes and an unsaturated magnetically induced luminescence effect of up to 200% (under 18 T). Studies confirmed that the luminescence enhancement mainly arises from magnetic-field-induced changes in ground-state spin population (amplitude modulation), rather than changes in excited-state lifetime, and for the first time experimentally verified the external heavy atom effect in polymeric radical luminophores.

Overall, luminescent diradicals, through structural design and electronic modulation, demonstrate rich photophysical properties and broad application potential in improving luminescence efficiency, achieving multiple emissions, and responding to external fields (magnetic, thermal), with particularly significant value in fields such as spin photonics, quantum information, and bioimaging.

The application of radicals in nanodiagnosis and therapy

Since the 21st century, cancer has evolved into a widespread public health crisis, imposing a lifelong clinical burden on diagnosed patients[71] The emergence of nanomedicine has driven significant advances in non-invasive treatment modalities in oncology research. Among emerging therapeutic paradigms, phototherapy—especially photodynamic therapy (PDT) and photothermal therapy (PTT)—has become a cutting-edge treatment due to its synergistic mechanisms and controllability.[72–74]

Stable luminescent radicals show significant potential in the field of tumor phototherapy. Through nanoencapsulation or chemical modification, the emission wavelength of luminescent radicals can be adjusted to the near-infrared (NIR) window I or II. Taking advantage of the weak absorption and scattering of biological tissues in this wavelength range, deeper tumor penetration and lower background fluorescence imaging can be achieved. In photodynamic therapy, their open-shell electronic structures can, through efficient energy or electron transfer pathways, generate reactive oxygen species dominated by singlet oxygen under light excitation, enabling oxidative killing of cancer cells and exhibiting unique adaptability to hypoxic microenvironments. Furthermore, they offer significant advantages in photothermal therapy. These molecules generally possess strong and broad near-infrared absorption bands and extremely high non-radiative transition rates, allowing absorbed light energy to be converted into heat almost without loss, thereby enabling precise tumor ablation. More importantly, as fully organic materials, they avoid the long-term toxicity risks associated with traditional metal-based photosensitizers or photothermal agents, and can further enhance biocompatibility, targeting, and circulation stability through nanoencapsulation. This provides an ideal material platform for achieving an integrated, efficient, and low-toxicity antitumor strategy. This section focuses on the multifunctional applications of nanoparticles constructed from stable luminescent radicals in fluorescence imaging-guided photodynamic therapy and photothermal therapy.

Fluorescence imaging

Near-infrared (NIR) fluorescence imaging has garnered significant attention in biomedical imaging due to its strong tissue penetration and low autofluorescence. Traditional NIR luminescent materials are predominantly closed-shell molecules, while organic luminescent radicals possess unique doublet characteristics—enabling fully spin-allowed transitions between excited and ground states—which theoretically allow for highly efficient emission. However, the application of these materials in bioimaging has been limited by their poor water solubility and susceptibility to emission quenching in aggregated states or polar environments.

In response to the issues of poor water solubility and fluorescence quenching in polar environments associated with this radical, Li[75] reported a novel red fluorescent nanoparticle based on the neutral luminescent radical **TTM-Cz-Br** and its precursor in 2022. The study employed the amphiphilic polymer DSPE-PEG2000 (Fig. 20a) to encapsulate the radical, and effectively suppressed aggregation-caused quenching through a strategy of doping with its precursor. The prepared nanoparticles exhibited uniform size (approximately 43.7 nm, Fig. 20d)), good stability in aqueous and phosphate-buffered saline environments, and bright red fluorescence (emission peak at 640 nm, Fig. 20c), achieving a photoluminescence quantum yield of 18.6%. Cell experiments demonstrated that the nanoparticles possessed low toxicity and excellent biocompatibility toward HCT116 cells (Fig. 20b). They were effectively taken up by the cells and successfully used for fluorescence imaging (Fig. 20e) in the cytoplasmic region.

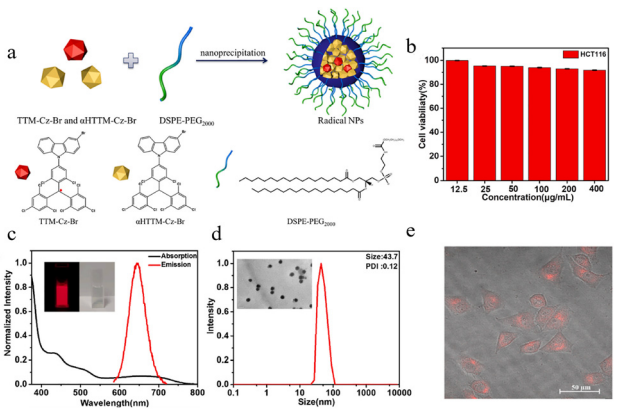

Fig. 20 (a) Radical NPs preparation. (b) HCT116 cell cytotoxicity of the radical NPs in the dark environment. (c) UV–Vis absorption and fluorescence spectra (375 nm excitation) of the radical NPs dispersed in PBS. (d) Hydrodynamic size of the radical NPs dispersed in DI water. The inset shows a TEM image of the radical NPs, and the scale bar is 200 nm. (e) Merge of bright-field image and red fluorescence channel, reproduced from ref. 75 with permission from Elsevier, *Dyes and Pigments*, 2022, 202, 110260, copyright 2022.

In 2023, this team developed another highly efficient near-infrared luminescence system based on **TTM-TPA** radicals,[76] providing an innovative solution for the application of luminescent radicals in the field of biology. This study constructed a D–A molecular structure using triphenylamine as the donor and tris(trichlorophenyl)methyl as the acceptor, successfully obtaining stable radicals with an emission wavelength exceeding 728 nm and a photoluminescence quantum yield of 24.4%. Theoretical calculations confirmed that the near-infrared emission originates from an intramolecular charge transfer excited state. To solve the aqueous quenching issue of this hydrophobic molecule, the researchers innovatively employed a nanoscale engineering strategy combining ''precursor doping'' and ''amphiphilic polymer encapsulation,'' packaging the radicals within DSPE-PEG2000 micelles. The resulting nanoparticles (approximately 115 nm in size, Fig. 21b) maintained good colloidal stability in aqueous solution, with an emission peak at 740 nm and a quantum yield of 9% (Fig. 21a). Cell experiments demonstrated that this nanoprobe exhibits excellent biocompatibility, can be successfully internalized by HCT116 cells, and produces clear near-infrared fluorescence signals in the cytoplasm (Fig. 21c–f). This work systematically proves that through the synergy of molecular design and nanotechnology, highly efficient luminescent radicals can be transformed into biocompatible near-infrared probes suitable for live-cell imaging, laying an important foundation for the development of radical-based theranostic agents.

To address the challenges of poor water solubility and susceptibility to quenching in polar environments for luminescent radicals, Arnold *et al.*[77] developed novel water-soluble **TTM** radical probes through ingenious molecular engineering. The study demonstrates that introducing oligoethylene glycol chains can impart excellent water solubility to **TTM** (Fig. 22a). The **TTM** derivative with carbazole as the donor (Compound **9**)

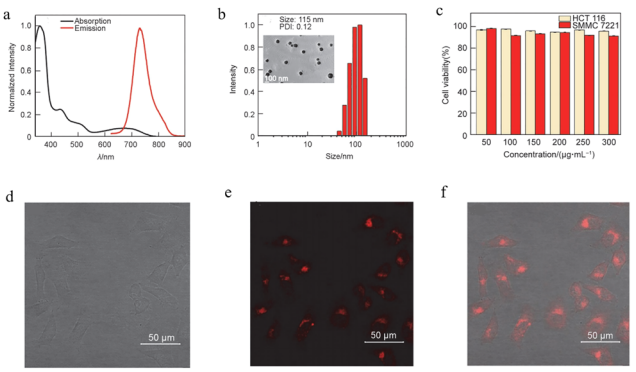

Fig. 21 (a) UV-Vis absorption and fluorescence spectra of **TTM**-TPA radical nanoparticle solution (deionized water). (b) Kinetic diameters of radical nanoparticles in PBS solution (the inset is a photograph taken by TEM). (c) MTT assay to detect the toxicity of radical nanoparticles to HCT116 cells and SMMC7221 cells. (d) Confocal imaging of **TTM**-TPA after co-incubation with HCT116 cells for 8 h in bright field. (e) **TTM**-TPA NIR fluorescence channel (700–800 nm). (f) **TTM**-TPA NIR fluorescence channel and bright field superimposed, reproduced from ref. 76 with permission from Springer Nature, *Chem. Res. Chin. Univ.*, 2023, 39, 192–196, copyright 2023.

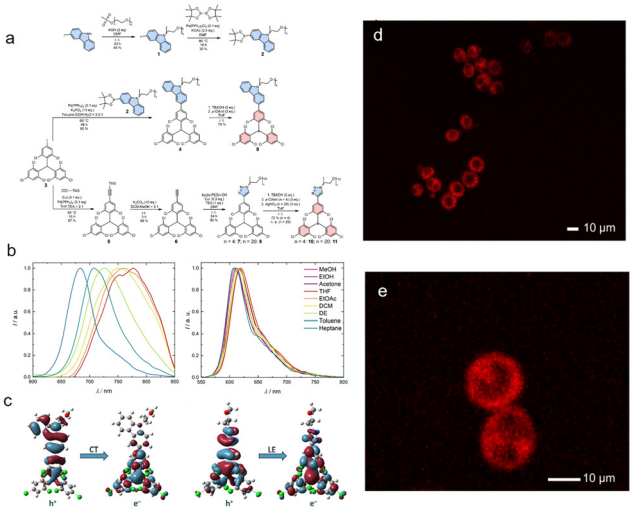

Fig. 22 (a) Synthesis of new OEG-functionalized **TTM** derivatives. (b) Emission spectra for solutions of radicals 9 (left) and 10 (right) in solvents of different polarity (0.1 ± 0.02 mM). (c) Natural transition orbitals (NTOs) for the $D_0 \rightarrow D_1$ transition in 9 (left) and 10 (right) in their ground state geometry. Confocal laser scanning micrographs of live cell macrophages incubated with radical 11. (d) Overview and (e) closeup on two macrophages with radical fluorescent dye, indicating that the radical 11 can be utilized for live cell staining, reproduced from ref. 77 with permission from MDPI, *Molecules*, 2024, 29, 995, copyright 2024.

exhibits a charge-transfer excited state (CT) (Fig. 22b and c), and its fluorescence is significantly quenched in polar and aqueous environments due to solvent stabilization effects. In contrast, derivatives with a locally excited state, constructed *via* click chemistry by introducing a triazole linker unit, show luminescence unaffected by solvent polarity (Fig. 22b and c). By extending the OEG chain to n = 20, the research team obtained a radical probe that combines high water solubility ($\geq$10 mg mL^{-1}) with stable red emission. Confocal microscopy imaging (Fig. 22d and e) confirmed that this molecular probe can be effectively internalized by macrophages and exhibits good biocompatibility. This work not only provides the critical ''locally excited state first'' design principle for developing radical luminescent materials suitable for aqueous bioimaging but also lays an important foundation for creating dual-mode molecular probes integrating fluorescence imaging and electron paramagnetic resonance detection.

PDT

In 2020, Cui[78] first reported a stable π-radical molecule (PTM-TPA, Fig. 23a) that forms nanoparticles through self-assembly and applied it as a novel photosensitizer to overcome hypoxic tumor environments in photodynamic therapy (PDT). The fluorescence emission peak of these nanoparticles is located in the near-infrared window at 800 nm. Light in this range has stronger tissue penetration and lower tissue autofluorescence background, providing an ideal optical window for deep tissue imaging and monitoring the treatment process (Fig. 23b). Traditional PDT relies on oxygen to generate singlet oxygen ($^1O_2$), but the tumor microenvironment is often hypoxic,

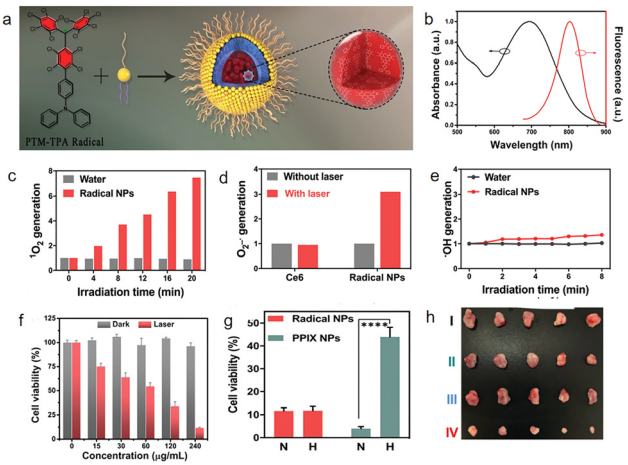

Fig. 23 (a) Nanoparticles of PTM-TPA; (b) UV-Vis absorption and fluorescence spectra (405 nm excitation) of the nanoparticles dispersed in PBS; (c) $^1O_2$ generation with and without the addition of radical NPs using SOSG as a probe; (d) $O_2^{-\bullet}$ generation by radical NPs using DHR123 as a probe; (e) •OH generation by radical NPs using HPF as a probe; (f) HeLa cell cytotoxicity of the radical NPs in the dark and under irradiation. (g) HeLa cell cytotoxicity of the radical NPs and PPIX NPs under normoxia (N) and hypoxia (H). (h) Representative images of tumors at day 14 after various treatments, reproduced from ref. 78 with permission from Royal Society of Chemistry, *Materials Horizons*, 2021, 8, 571–576, copyright 2021.

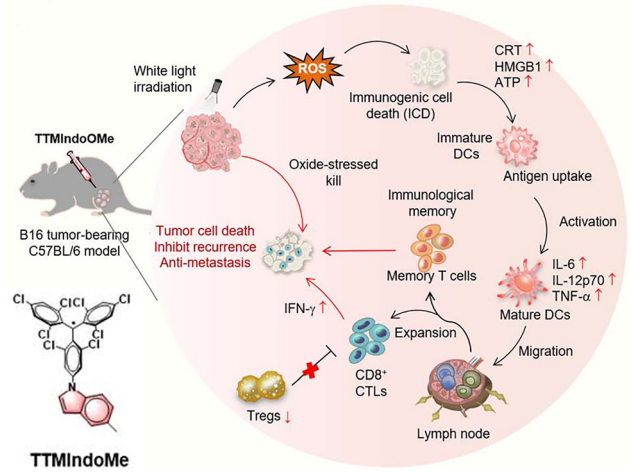

Fig. 24 Schematic mechanism of **TTM**IndoOMe for photodynamic immunotherapy of a B16 tumor-bearing C57BL/6 model *in vivo*, reproduced from ref. 79 with permission from Royal Society of Chemistry, *Chemical Science*, 2024, 15, 6421–6431, copyright 2024.

severely limiting therapeutic efficacy. Under 635 nm laser irradiation, these radical nanoparticles can not only generate $^1O_2$ *via* energy transfer under normal oxygen conditions, but also continuously produce superoxide radicals ($O_2^{-\bullet}$) through an electron transfer pathway under hypoxic conditions, achieving an oxygen-independent type I PDT mechanism, thus effectively overcoming the inhibitory effect of tumor hypoxia on therapy. Without light exposure, even high concentrations of the radical NPs show almost no toxicity to HeLa cells, demonstrating their good biocompatibility. Under light exposure, radical NPs efficiently kill cancer cells under both normoxic (N) and hypoxic (H) conditions, with no significant difference between the two. In contrast, traditional photosensitizer PPIX nanoparticles show severely reduced efficacy under hypoxic conditions, directly demonstrating the unique advantage of radical NPs in overcoming hypoxia. During a 14-day treatment period, only the "NPs + laser (L)" group completely suppressed tumor growth, with volumes no longer increasing and ultimately nearly disappearing (Fig. 23h), indicating excellent antitumor efficacy.

In 2024, Wang[79] developed a stable luminescent radical **TTMIndoOMe** (Fig. 24) and applied it to overcome tumor hypoxia in photodynamic immunotherapy, demonstrating its multiple applications in bio-nano diagnosis and treatment. The treatment process is shown in Fig. 24, as an efficient type-I photosensitizer, it can continuously generate superoxide anion radicals under white light irradiation through an electron transfer mechanism using the inherent unpaired electrons in the molecule. This process is almost unaffected by oxygen concentration, enabling effective overcoming of the hypoxic tumor microenvironment and achieving efficient direct cell killing. More importantly, **TTMIndoOMe**-mediated photodynamic therapy can strongly induce immunogenic cell death, prompting tumor cells to release 'danger signals' such as ATP and HMGB1 and expose calreticulin, thereby turning apoptotic cancer cells into 'endogenous vaccines.' This process can systematically activate anti-tumor immunity: promoting dendritic cell maturation, recruiting and activating cytotoxic $CD8^+$ T cells to infiltrate tumors, while inhibiting immunosuppressive regulatory T cells, and inducing the generation of memory T cells with long-term protective potential. Therefore, this molecule cleverly integrates three functions—hypoxia-insensitive therapeutic agent, immune alert trigger, and systemic immune activator—into one, providing an innovative strategy for developing a next-generation nano-diagnostic and therapeutic platform capable of simultaneously combating tumor hypoxia and immune suppression.

In the same year, to overcome the oxygen dependence of traditional photosensitizers and the scarcity of near-infrared (NIR) molecules, Li[80] successfully developed two novel type-I photosensitizer nanoparticles, TTM-3PDMAC:HTTM-3PDMAC@NPs and TTM-PDMAC:HTTM-PDMAC@NPs, by integrating luminescent radicals with their precursors (Fig. 25a). This work employed DSPE-PEG2000 encapsulation technology to disperse hydrophobic radicals within the matrix of their precursors, effectively addressing the issues of poor water solubility and aggregation-induced fluorescence quenching of the radicals, thereby preserving their NIR emission properties—with maximum emission peaks at 785 nm and 730 nm, respectively. Studies demonstrated that upon light irradiation, these nanoparticles could generate reactive oxygen species (ROS), particularly superoxide anions (O_2^{-}) (Fig. 25c), *via* a type-I photodynamic mechanism. Notably, this process originated from the synergistic interaction between the radicals and their precursors, enabling efficient ROS production under both normoxic and hypoxic conditions. *In vitro* experiments confirmed the favorable

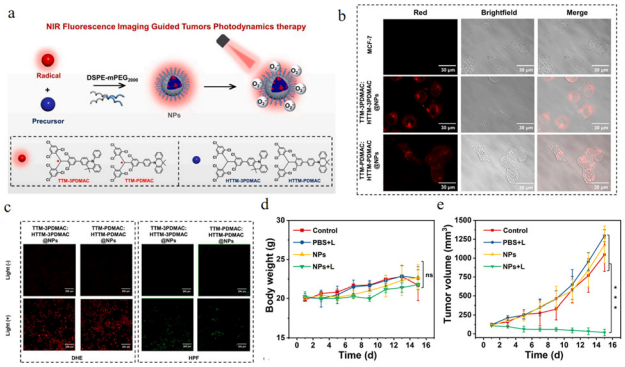

Fig. 25 (a) Preparation of type-I PSs (NPs). (b) CLSM images of **TTM**-3PDMAC:H**TTM**-3PDMAC@NPs and **TTM**-PDMAC:H**TTM**-PDMAC@NPs in MCF-7 cells. (c) The intracellular ROS production capacity of **TTM**-3PDMAC:H**TTM**-3PDMAC@NPs and **TTM**-PDMAC:H**TTM**-PDMAC@NPs (100 μg mL^{-1}) was tested using DHE and HPF (10 μM), scale bar is 200 μm. (d) Body weight of mice (n = 5). (e) Changes in relative tumor volume over 15 days for the different treatments of tumor-bearing mice (n = 5), data expressed as mean ± s.d, ***$P < 0.001$, reproduced from ref. 80 with permission from Elsevier, *Sensors and Actuators B: Chemical*, 2024, 414, 135931, copyright 2024.

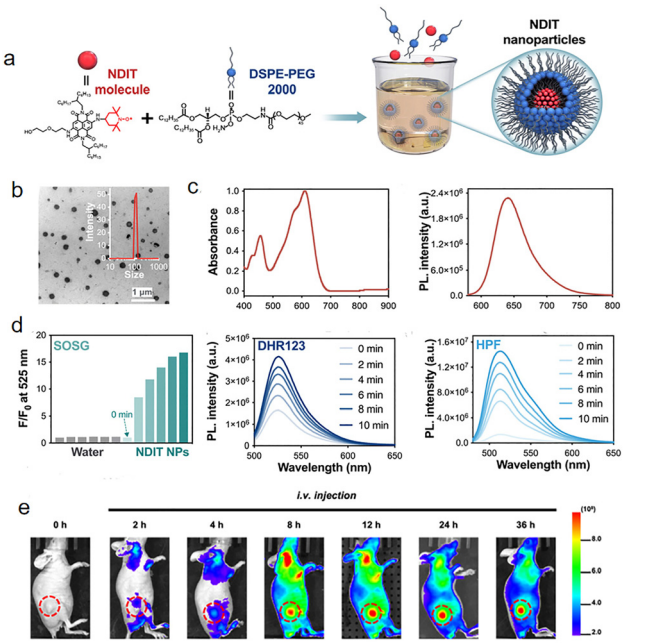

Fig. 26 (a) Scheme of NDIT nanoparticle preparation. (b) TEM image of NDIT NPs, the inset shows the zoomed-in hydrodynamic size by DLS. (c) Absorption and fluorescence spectra of aqueous NDIT NP solution. (d) Use SOSG, DHR123, and HPF probes respectively, and measure the concentrations of $^1O_2$, $O_2^{-\bullet}$, and $^\bullet OH$ every two minutes. (e) FLI of tumors after i.v. injection of NPs at various time periods (the location of tumors is highlighted with a red dashed line), reproduced from ref. 81 with permission from Royal Society of Chemistry, *Materials Horizons*, 2025, 12, 1002-1007, copyright 2025.

biocompatibility and phototoxicity of the nanoparticles (Fig. 25d and e), showing significant photodynamic killing effects across multiple cancer cell lines. Furthermore, in a 4T1 tumor-bearing mouse model, TTM-3PDMAC:HTTM-3PDMAC@NPs exhibited excellent tumor-targeting accumulation, NIR imaging-guided functionality (Fig. 25b), and remarkable tumor suppression efficacy, with minimal systemic toxicity and no observable pathological damage in major organs.

In 2025, Cui[81] covalently attached the commercialized, highly stable 2,2,6,6-tetramethylpiperidine-1-oxyl (TEMPO) radical units to the naphthalene diimide (NDI) molecular backbone. Utilizing TEMPO's inherent unpaired electrons as 'electron donors,' they conveniently created a stable radical photosensitizer in a one-step process. The nanoparticles (NDIT NPs) self-assembled from this molecule (Fig. 26a) have an average particle size of 100 nm (Fig. 26b), and exhibit absorption and emission peaks at 600 nm and 641 nm (Fig. 26c and d). These nanoparticles demonstrate a rare and comprehensive ability to generate reactive oxygen species (ROS) when exposed to a 635 nm laser: they can not only generate type II singlet oxygen ($^1O_2$) through energy transfer, but also efficiently generate type I superoxide anion ($O_2^{-\bullet}$) and hydroxyl radical ($^\bullet OH$) through electron transfer (Fig. 26d and c). This 'dual type I and type II mechanism' feature enables it to effectively tackle the complex tumor microenvironment. Under normoxic conditions, multiple ROS synergistically enhance the effect; under hypoxic conditions, the type I pathway (electron transfer) remains unaffected, continuously producing $O_2^{-\bullet}$ and $^\bullet OH$, thus overcoming the oxygen dependency limitation of traditional PDT. Furthermore, these nanoparticles demonstrated high antitumor efficacy both *in vitro* and *in vivo*, with good tumor-targeting accumulation in tumor-bearing mice (peaking 12 hours after injection). In the group treated with NDIT NPs combined with laser irradiation, tumors were nearly completely eradicated within 14 days (Fig. 26e), showing results far superior to all control groups. Meanwhile, the mice maintained stable body weight, with no pathological damage in major organs and normal blood biochemical parameters, demonstrating excellent biosafety and therapeutic specificity.

Diradical molecules contain two unpaired electrons, which gives their ground state the highly reactive open-shell characteristic. Under photoexcitation, this structure can produce reactive oxygen species through a more efficient electron transfer pathway (Type I mechanism), particularly excelling at generating superoxide anions and hydroxyl radicals. Compared with traditional photosensitizers that rely on energy transfer (Type II mechanism) to produce singlet oxygen, the Type I mechanism is insensitive to the hypoxic environments commonly found within solid tumors, thereby overcoming a key limitation of conventional PDT.

In 2024, our team[82] discovered a stable organic diradical molecule, TFC-I, with aggregation-induced emission (AIE) characteristics, exhibiting strong fluorescence emission in the near-infrared region. As shown in Fig. 27, when integrated into amphiphilic peptide nanoparticles P-TI, P-TI showed significant advantages: high photostability, aggregation-induced emission, bright near-infrared fluorescence, considerable quantum yield, strong near-infrared two-photon absorption, and excellent reactive oxygen species (ROS) generation capability. Under 800 nm laser excitation, P-TI exhibited a two-photon

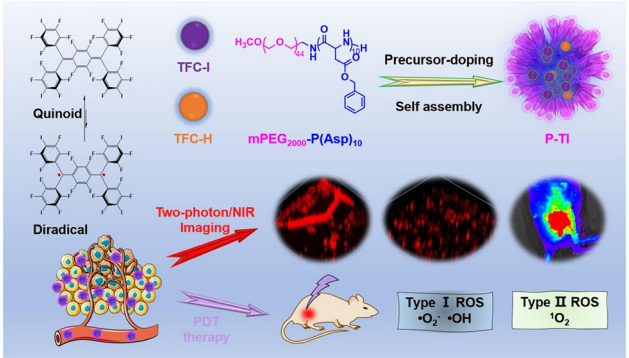

Fig. 27 Organic stable diradicaloid encapsulated by polypeptide nanoparticles for NIR two-photon phototheranostics, reproduced from ref. 82 with permission from American Chemical Society, *ACS Applied Materials & Interfaces*, 2024, 16, 59907–59920, copyright 2024.

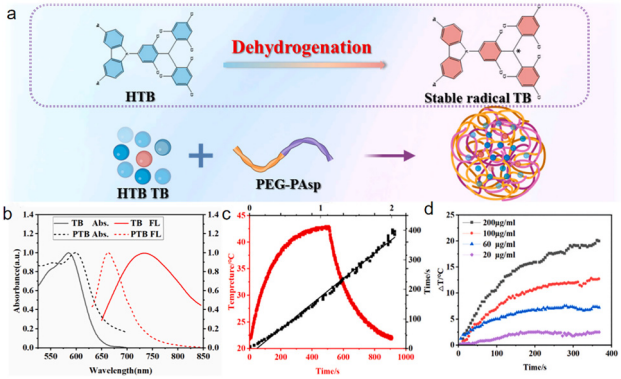

Fig. 28 (a) Preparation of TB nanoparticles. (b) Absorption and emission spectra of TB in THF and PTB in water. (c) Calculation of PCE of NPs. (d) Temperature curves of NPs with different concentrations, reproduced from ref. 83 with permission from Elsevier, *Talanta*, 2024, 266, 124948, copyright 2024.

absorption cross-section of approximately 400 GM and a fluorescence quantum yield of 37%, achieving high-brightness, high-contrast near-infrared two-photon imaging. In tissue penetration experiments, the imaging depth reached 0.95 mm, outperforming most previously reported two-photon dyes, making it suitable for high-resolution three-dimensional imaging of deep tumors. Additionally, P-TI could efficiently generate ROS under light, with a total ROS generation efficiency significantly higher than commercial photosensitizers TPP and Ce6 (about 5–8 times). Moreover, P-TI can simultaneously produce Type I ($^{\bullet}O_2^-$, $^{\bullet}OH$) and Type II ($^1O_2$) ROS, exhibiting hypoxia resistance and suitability for the tumor microenvironment. P-TI can specifically target mitochondria, enhancing the cytotoxicity of photodynamic therapy. *In vitro* experiments showed low cytotoxicity in the dark and effective induction of cancer cell apoptosis under irradiation. In animal studies, P-TI suppressed tumor growth by 67% under light exposure and showed no significant toxicity to major organs, demonstrating good biocompatibility. In summary, P-TI achieves high-resolution visualization and precise treatment of deep tumors through the synergistic effect of two-photon imaging and photodynamic therapy, providing a new strategy for the application of organic radical materials in the biomedical field.

PTT

In 2023, our team reported[83] a novel carbon-centered organic radical molecule TB (3,6-dibromo carbazole-modified tri(2,4,6-trichlorophenyl)methyl radical), which was encapsulated with amphiphilic peptide mPEG2000-P (Asp)10 using a 'precursor doping' strategy to construct a multifunctional nano-diagnosis and therapy platform PTB (Fig. 28a). These nanoparticles exhibit a fluorescence quantum yield of up to 18.68% in the near-infrared region I (emission around 750 nm, Fig. 28b), suitable for high-brightness, high-contrast real-time tumor fluorescence imaging. After intravenous injection, they effectively accumulate in tumor sites (peaking at 24 hours), providing precise spatiotemporal guidance for treatment. Under 635 nm laser irradiation, PTB simultaneously generates type I (superoxide anion $O_2^{-\bullet}$) and type II (singlet oxygen $^1O_2$) reactive oxygen species, overcoming the limitations of tumor hypoxic microenvironments for traditional PDT. Moreover, PTB exhibits excellent photothermal conversion efficiency (42.39%, Fig. 28c), and irradiation of a 200 mg mL^{-1} PTB solution for 10 minutes can raise the temperature by over 20 °C (Fig. 28d); in other words, the body temperature of mice can increase from 30 °C to about 50 °C, effectively inducing thermal ablation of tumor cells. *In vitro* experiments show that PTB has low dark toxicity and strong cytotoxicity against 4T1 and HepG2 cancer cells under light exposure. In the 4T1 tumor-bearing mouse model, PTB-mediated synergistic therapy significantly inhibited tumor growth. H&E staining showed extensive necrosis of tumor tissues, while no obvious damage was observed in major organs, demonstrating excellent biocompatibility. This work provides solid experimental evidence for PTB as a novel organic radical-based integrated diagnosis and therapy platform.

In 2024, our team further explored the multifaceted innovative applications of stable organic radical molecules (CNPP)[84] and their peptide-based nanoparticles (PCNPP) in bionanodiagnostics and therapy. Firstly, as a near-infrared II (NIR-II, 1000–1200 nm) fluorescent probe, CNPP exhibits a fluorescence quantum yield as high as 0.86%, significantly surpassing most known NIR-II organic dyes. Its nanoparticles, PCNPP, demonstrate excellent accumulation properties and high-contrast imaging capabilities *in vivo*, allowing for long-lasting, high signal-to-noise fluorescence imaging at tumor sites, providing a powerful tool for precise localization and real-time monitoring. Secondly, this nanosystem features a "self-enhancing" photothermal conversion property. As shown in Fig. 29, CNPP molecules exhibit a temperature-sensitive reversible dimerization–dissociation equilibrium: as the local temperature rises, more radicals are generated, further enhancing the photothermal effect and increasing the photothermal conversion efficiency from 43.5% to 57.5%. This mechanism enables effective photothermal therapy (PTT) at lower drug concentrations and laser power, improving the safety and feasibility of treatment. More importantly, PCNPP can be used for mild photothermal

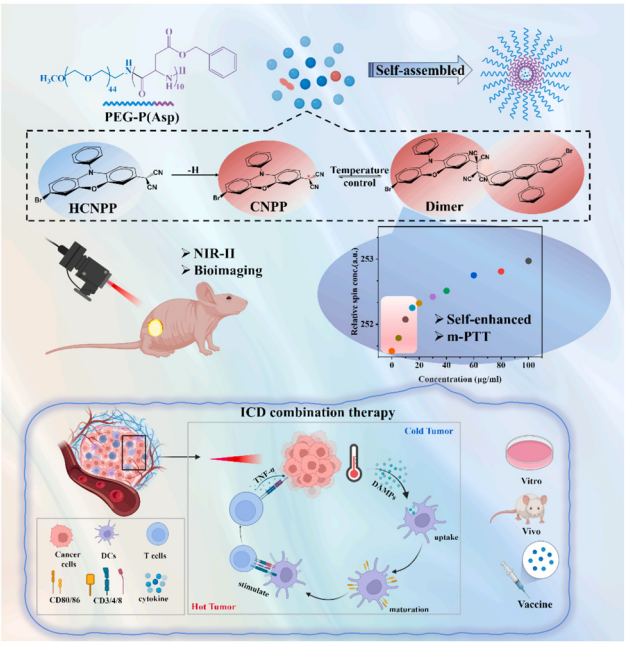

Fig. 29 CNPP is used as a dye and photosensitizer for NIR imaging-guided fluorescence imaging and mild photothermal therapy, reproduced from ref. 84 with permission from Elsevier, *Journal of Colloid and Interface Science*, 2024, 669, 578–589, copyright 2024.

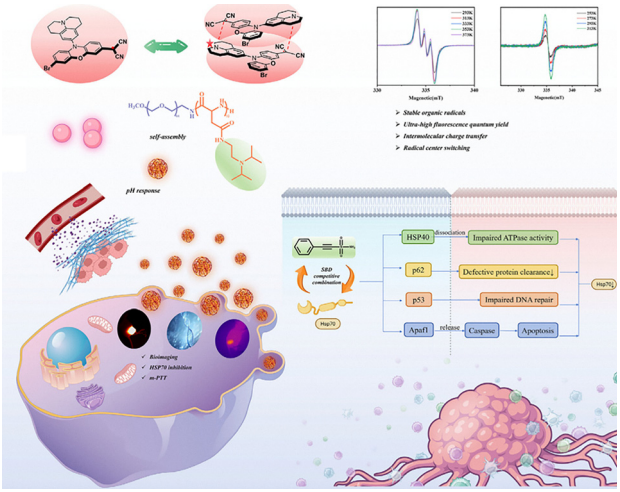

Fig. 30 Schematic diagram of CNPJ properties and their application in tumor phototheranostics, reproduced from ref. 50 with permission from Wiley, Angew. Chem., Int. Ed., 2025, 64, e202509609, copyright 2025.

therapy (m-PTT, 40–45 °C), which avoids damage to normal tissues while promoting the release of damage-associated molecular patterns (DAMPs) such as CRT and HMGB1 through fractionated irradiation, inducing immunogenic cell death (ICD, Fig. 29). This mild hyperthermia not only directly kills tumor cells but also activates dendritic cells and T cells, transforming "cold tumors" into "hot tumors" and enhancing antitumor immune responses. Additionally, the study further utilized tumor cells treated with PCNPP to prepare an immune-stimulatory tumor vaccine, which demonstrated the potential to inhibit distant tumor growth and metastasis in animal models, offering a new strategy for tumor immunotherapy.

In 2025, through further exploration, our team[50] successfully synthesized the dicyanomethyl radical derivative CNPJ (Fig. 30a). By introducing a julolidine group to modulate the electronic structure, it demonstrated multifunctional synergistic applications in biological nanotheranostics. First, CNPJ exhibits ultra-bright near-infrared II (NIR-II) fluorescence imaging capability, with an absolute fluorescence quantum yield as high as 2.57%, which is a rare high value among NIR-II emitters. This enables high-resolution, high-contrast imaging of blood vessels and tumors *in vivo*, supporting precise localization and real-time monitoring. Second, CNPJ has a temperature-sensitive reversible monomer-π dimer equilibrium (Fig. 30a and b), which endows it with a self-enhancing photothermal conversion capability. Under 808 nm laser irradiation, its nanoparticles (PJ NPs) achieve a photothermal conversion efficiency of 49.33% and can still perform efficient mild photothermal therapy (m-PTT) within moderate temperature ranges (<48 °C), reducing damage to normal tissues. As shown in Fig. 30c, to further overcome potential thermoresistance of tumor cells during mild hyperthermia, the team co-loaded the heat shock protein inhibitor PES with CNPJ in pH-responsive amphiphilic polymer nanoparticles. As shown, under the acidic conditions of the tumor microenvironment, PES is released in a controlled manner, effectively inhibiting the chaperone function of HSP70, significantly enhancing the cell-killing effect of mild photothermal therapy. In animal models, this nanoplatform exhibits excellent tumor-targeted accumulation, with fluorescence signals continuously increasing at tumor sites, providing an ideal therapeutic time window. The PES-combined mild phototherapy group (PJ@PES L+) achieved over 94% tumor elimination, with no significant recurrence or metastasis observed, demonstrating outstanding antitumor efficacy and biocompatibility. In summary, the CNPJ-based nanotheranostic system successfully integrates high-brightness NIR-II imaging, self-enhancing mild photothermal therapy, and thermoresistance-reversal strategies, achieving an integrated "diagnosis–treatment–enhancement" approach and providing new insights for precise tumor therapy and nanomedicine design.

In recent years, the advantages of diradicals in photothermal therapy have also been explored. The double radicals 2PhNVDPP and PhNVDPP[64] (Fig. 31a) reported by the Feng *et al.* in 2024 represent an important breakthrough in organic open-shell materials in the field of nanomedicine. After forming water-dispersible 2PhNVDPP NPs through nano-encapsulation, their maximum emission wavelength reached 1013 nm and extended to 1300 nm (Fig. 31b), successfully entering the second near-infrared window. These nanoparticles exhibited a good signal-to-noise ratio under various long-pass filters at 900 nm, 1000 nm, 1100 nm, and 1300 nm, with the signal-to-background ratio at the 1300 nm window reaching as high as 5.03, achieving high-contrast deep tissue vascular imaging. In the 4T1 tumor-bearing mouse model, 2PhNVDPP NPs reached maximum accumulation at the tumor site 9 hours post-injection (Fig. 31c), providing precise imaging guidance for selecting subsequent

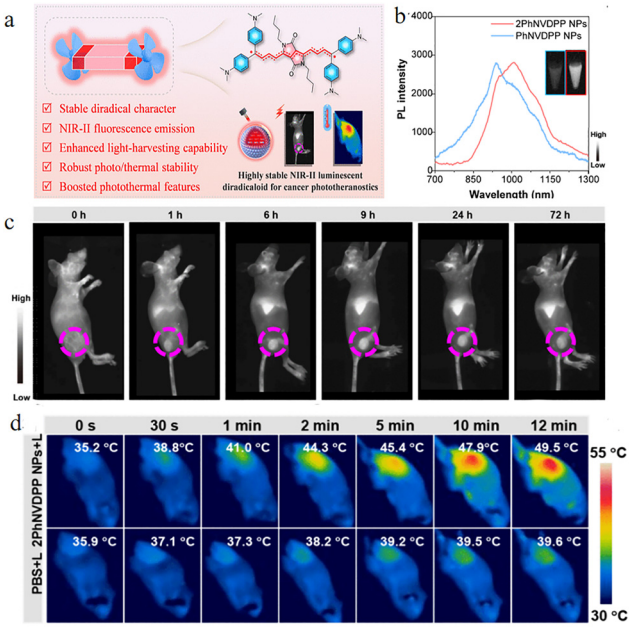

Fig. 31 (a) Design concept of 2PhNVDPP NPs. (b) PL spectra of PhNVDPP NPs and 2PhNVDPP NPs in aqueous solution. (c) NIR-II fluorescence imaging of tumors in living mice at different time points after 2PhNVDPP NP injection. The tumor region is indicated with a purple dashed circle. (d) Schematic illustration showing the photothermal therapy process for *in vivo* 4T1 breast tumor-bearing mice, reproduced from ref. 64 with permission from American Chemical Society, *Journal of the American Chemical Society*, 2024, 146, 32582–32594, copyright 2024.

treatment timing. 2PhNVDPP NPs have a molar extinction coefficient of up to 1.8×10^4 M^{-1} cm^{-1} at 808 nm, with a photothermal conversion efficiency of 53%. In *in vitro* experiments, after these nanoparticles were targeted and accumulated in mitochondria, irradiation with an 808 nm laser effectively induced apoptosis in cancer cells, with a half-maximal inhibitory concentration of approximately 28 μM. In *in vivo* treatment, the local tumor temperature rapidly rose from 35.2 °C to 44.3 °C within 2 minutes of laser irradiation and eventually stabilized at around 49.5 °C (Fig. 31d), achieving complete tumor ablation, with no recurrence observed during a 15-day observation period. Moreover, the nano-encapsulation not only solves the water dispersibility problem of the diradical molecules but also significantly enhances their stability under light exposure, thermal cycling, and physiological conditions. The 2PhNVDPP NPs maintain stable photothermal performance after five laser on–off cycles, and there are no significant changes in their absorption spectrum or particle size in different biological oxidative-reductive environments. Systematic *in vivo* and *in vitro* safety evaluations indicate that even at high concentrations, they do not cause noticeable liver or kidney function damage or systemic inflammatory responses, demonstrating good biocompatibility.

In 2025, Liu reported a Chichibabin molecule[85] and applied it to photothermal therapy (Fig. 32a). **TT-CzPh** has a maximum emission wavelength of 821 nm and a photoluminescence quantum yield of 6.4%, significantly higher than its precursor **TTM-TTM** (0.8%) (Fig. 32b). After forming water-dispersible **TT-CzPh** nanoparticles (NPs) through nano-encapsulation, it still maintains bright near-infrared fluorescence. In the 4T1 tumor-bearing mouse model, the nanoparticles specifically accumulate at the tumor site after injection, with the fluorescence signal peaking at 9 hours (Fig. 32c), providing precise spatiotemporal guidance for subsequent photothermal therapy. The **TT-CzPh** molecule itself has a photothermal conversion efficiency of up to 87.5%, and after being nano-formulated (**TT-CzPh** NPs), it still maintains a high efficiency of 82%. Under 655 nm laser irradiation, the temperature of the nanoparticle solution and the local tumor area can rapidly reach an effective ablation temperature (>50 °C) (Fig. 32d and e). *In vitro* experiments show that after laser irradiation, the cancer cell survival rate can drop to around 5%, inducing a decrease in mitochondrial membrane potential and leading to cell apoptosis. **TT-CzPh** NPs have an average particle size of about 109 nm and carry a negative surface charge, which facilitates their accumulation in tumor sites through the EPR effect. *In vivo* and *in vitro* toxicity assessments showed that, without laser irradiation, the nanoparticles exhibit very low toxicity to normal tissues and cells (Fig. 32f–h). During the

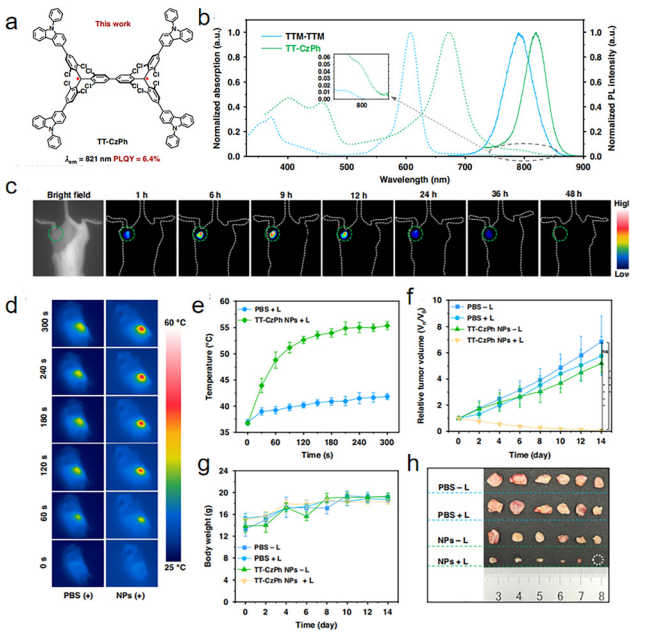

Fig. 32 *In vivo* fluorescence imaging and photothermal therapy of **TT-CzPh** NPs. (a) Molecular structure of **TT-CzPh**. (b) Absorption and emission spectra of **TT-CzPh**. (c) NIR fluorescence imaging of tumors in living mice at different time points after **TT-CzPh** NPs injection. The tumor region is indicated with a green dashed circle. (d) Temperature changes at tumor sites with increasing time under continuous laser irradiation after treatment with PBS and **TT-CzPh** NPs. (e) Thermal images of mice 9 h postinjection of the **TT-CzPh** NPs aqueous solution under 655 nm laser irradiation (1.0 W cm^{-2}) for 5 min (n = 6). (f) Average relative tumor volume (RTV) of mice after different formulations (n = 6; $^*P < 0.05$, $^{**}P < 0.01$, $^{***}P < 0.001$, $^{****}P < 0.0001$). (g) Average body weights of mice over a 14-day period for different treatment groups (n = 6). (h) Images of tumors extracted from 4T1 tumor-bearing mice *ex vivo* after 14 days of treatment, reproduced from ref. 85 with permission from Springer Nature, *Light: Science & Applications*, 2025, 14, 289, copyright 2025.

14-day treatment period, the body weight of mice in the treatment group remained stable, no significant pathological damage was observed in major organs, and there was no tumor recurrence after complete eradication. Systematic hematological and biochemical analyses further confirmed their excellent biocompatibility.

In the same year, Zeng[86] reported on the dual-radical system **DD-1–3** (Fig. 33a), with a maximum emission wavelength extending up to 1250 nm, fully entering the NIR-II region (Fig. 33b). Photons in this wavelength range exhibit lower tissue scattering and absorption, allowing them to penetrate thicker biological tissues and achieve deep, high-resolution *in vivo* imaging. As shown in the Fig. 33c, after being encapsulated into nanoparticles, **DD-1** produced a bright NIR-II fluorescence signal at the subcutaneous injection site in mice that was 9 times stronger than that of the blank control group, demonstrating its outstanding potential for *in vivo* imaging. These diradical compounds not only emit light, but their strong near-infrared absorption makes them efficient photothermal conversion agents. Furthermore, the research found that after nanoparticles were injected into mice, when exposed to a 10-minute laser irradiation at 808 nm (0.5 W cm^{-2}), the temperature rose rapidly from 36.2 °C to 52.8 °C (Fig. 33d). Fig. 30e show that **DD-1** nanoparticles can efficiently convert light to heat under 808 nm laser irradiation, raising the solution temperature from 20 °C to 71 °C within 5 minutes, with a measured photothermal conversion efficiency of up to 49%. This high-efficiency thermal effect can directly induce apoptosis or necrosis in tumor cells. *In vitro* cell experiments confirmed that after laser irradiation, **DD-1** nanoparticles can effectively kill 4T1 cancer cells, and they exhibit good photothermal stability, withstanding multiple heating/cooling cycles. Under conditions without light, **DD-1** nanoparticles exhibit very low toxicity to cells, even at high concentrations. In summary, these organic diradicals, designed through symmetry breaking and ICT regulation, successfully integrate key advantages such as deep-penetrating NIR-II imaging, efficient photothermal conversion, combined diagnosis and therapy, as well as good biocompatibility and stability. They provide a highly promising material basis for developing a new generation of high-performance, intelligent tumor diagnosis and treatment platforms, representing a significant breakthrough for organic functional molecules in the forefront of biomedical applications.

In the same year, Li[87] rationally designed donor (D)–acceptor (A) structures to synthesize a series of neutral π-radical molecules with excellent stability, among which **SFA-BTM** exhibited the most outstanding performance. This work

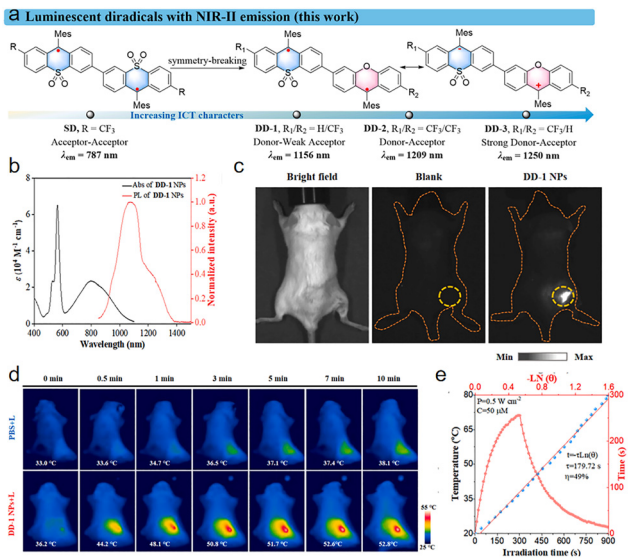

Fig. 33 (a) Molecular Design of **DD-1–3**. (b) UV-vis-NIR absorption and PL spectra of **DD-1** NPs in aqueous solution excited by an 808 nm laser (1×10^{-4} M). (c) NIR-II fluorescence imaging photographs of **DD-1** NPs subcutaneous injection in a BALB/c mouse, taken with 1000 nm long-pass filters under 808 nm laser excitation. (d) Infrared thermal images captured *in vivo* for PBS and **DD-1** NPs groups under 808 nm laser irradiation (0.5 W cm^{-2}). (e) Photothermal heating and cooling curves of **DD-1** NPs with respect to the linear fitting ln(*θ*) *versus* cooling time, reproduced from ref. 86 with permission from Cell Press (Elsevier), *Chem*, 2025, 11, 102621, copyright 2025.

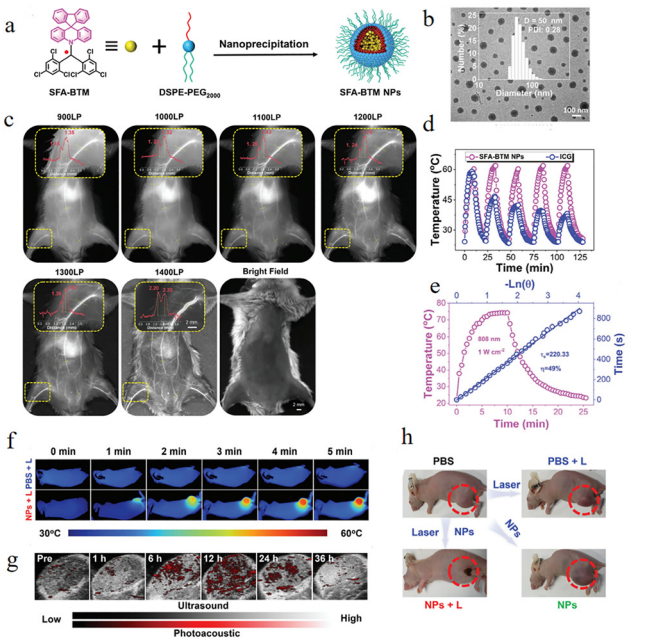

Fig. 34 (a) Schematic illustration of the fabrication of **SFA-BTM** NPs. (b) The image of visualization of the morphology of **SFA-BTM** NPs characterized by TEM, scale bar = 100 nm. Insert graph: size distribution of the **SFA-BTM**. (c) Whole-body NIR-II bioimaging with sequential LP filters from 1000 to 1400 nm. Inset: NIR bioimaging and SBR analysis of the labeled vessel under different LP filters. (d) Photothermic resistance capabilities of the **SFA-BTM** NPs and ICG upon 808 nm laser illumination (1 W cm^{-2}) for five cycles (each cycle contains 10 min irradiation and 10 min cooling). (e) Curves of photothermal heating and cooling until room temperature of **SFA-BTM** NPs aqueous solution, and linear analysis of PCE according to the cooling process NPs dispersed in water. (f) Photothermal images of 143B tumor-bearing mice in different treatment groups (**SFA-BTM** NPs: 10 mg kg^{-1}) under 808 nm laser irradiation (1 W cm^{-2}). (g) Photoacoustic images of tumor location at the post-intravenous injection of **SFA-BTM** NPs. (h) Comparative photographs of 143B tumor-bearing mice after various treatments, reproduced from ref. 87 with permission from Wiley, *Advanced Science*, 2025, 12, 2411733, copyright 2025.

marked the first successful application of **TTM**-based radicals in photothermal theranostics. **SFA-BTM** demonstrated strong absorption in the first near-infrared (NIR-I) region at 716 nm, with its absorption tail extending to 1000 nm, and exhibited distinct fluorescence emission in the NIR-II region (1000–1700 nm). The molecule possessed excellent photostability and thermal stability, achieving a high photothermal conversion efficiency (PCE) of 49% (Fig. 34e), surpassing many previously reported photothermal materials. Using DSPE-PEG2000 encapsulation technology, the researchers further prepared water-dispersible **SFA-BTM** nanoparticles (NPs) (Fig. 34a) with a diameter of approximately 50 nm (Fig. 34b), which showed good colloidal stability and biocompatibility. Under 808 nm laser irradiation, these nanoparticles exhibited remarkable photothermal heating performance and cyclic photothermal stability (Fig. 34c). In biological applications, **SFA-BTM** NPs achieved high-resolution whole-body NIR-II angiography for the first time, clearly visualizing the abdominal vascular network in mice. Additionally, they demonstrated good photoacoustic imaging (PAI) and photothermal imaging capabilities (Fig. 34f and g), enabling effective monitoring of nanoparticle accumulation and temperature changes at tumor sites. In terms of therapy, **SFA-BTM** NPs showed significant photothermal killing effects on various tumor cells *in vitro* and achieved effective tumor ablation in an orthotopic bone tumor model (Fig. 34h), while simultaneously inhibiting tumor-associated bone erosion and promoting bone repair. *In vivo* experiments confirmed low systemic toxicity of the nanoparticles, with no pathological damage observed in major organs and normal blood biochemical parameters, indicating high biosafety. This study provides a new molecular design strategy and experimental foundation for developing sustainable, stable, and efficient organic radical-based NIR-II theranostic agents, advancing the development of integrated platforms for photothermal therapy and multimodal imaging.

Outlook

Stable luminescent radicals, as emerging organic functional molecules, have broad and profound prospects in the field of nano-diagnosis and therapy, with the potential to achieve multidimensional breakthroughs—from materials and technology to application paradigms.

The core of future research lies in systematically addressing current bottlenecks and unleashing their unique potential through multidisciplinary ''nanoengineering''.

(1) In the realm of material design and delivery, developing smart responsive nanocarriers (such as pH-, enzyme-, or redox-responsive) can enable tumor microenvironment-triggered high-precision drug release, maximizing therapeutic efficacy while minimizing systemic toxicity. At the same time, utilizing the modifiability of radical molecules and coupling them with targeting peptides or antibody fragments can create actively targeted ''nano-missiles'', significantly enhancing accumulation efficiency at tumor sites.

(2) In integrating diagnostic and therapeutic functions, their advantages can be fully realized. Based on radicals' efficient Type I photodynamic activity and intrinsic near-infrared fluorescence/phosphorescence, a truly ''theranostic'' platform can be constructed: fluorescence imaging can guide localization before treatment; during photodynamic therapy, changes in emission intensity or lifetime can reflect local reactive oxygen species concentration or oxygen levels in real-time and *in situ*, thus dynamically monitoring the treatment process and enabling dose regulation; after treatment, their photothermal effect can be used for thermal imaging to assess ablation effectiveness. This closed-loop system integrating diagnosis, therapy, and efficacy monitoring will greatly advance precision medicine.

(3) A more cutting-edge direction is developing innovative therapies leveraging their spin properties. Their magnetic responsiveness can not only be used for contrast enhancement in magnetic resonance imaging (MRI) but also combined with external physical fields (such as alternating magnetic fields or microwaves) to create new models of remote, deep, precision therapy through ''magnetothermal-photodynamic'' synergistic treatment or ''microwave modulation''. Moreover, the spin state of radicals, as readable and writable quantum information units, provides long-term potential for bio-based quantum sensing technologies, potentially detecting extremely subtle biochemical changes *in vivo*.

Although challenges remain in long-term *in vivo* stability, clear metabolic pathways, and large-scale standardized production, with the deep integration of organic synthetic chemistry, nanotechnology, and clinical medicine, stable luminescent radicals are expected to surpass traditional inorganic or metal-based materials, leading the next generation of intelligent, efficient, low-toxicity, and functionally programmable nano-diagnostic and therapeutic systems.

Conflicts of interest

We have no conflicts of interest.

Data availability

Data will be provided on the requirement.

Acknowledgements

This work is supported by the National Natural Science Foundation of China (No. 52373159).

Notes and references

1 Z. Cui, A. Abdurahman, X. Ai and F. Li, *CCS Chem.*, 2020, **2**, 1129–1145.
2 A. Mizuno, R. Matsuoka, T. Mibu and T. Kusamoto, *Chem. Rev.*, 2024, **124**, 1034–1121.
3 N. Aizawa, Y.-J. Pu, Y. Harabuchi, A. Nihonyanagi, R. Ibuka, H. Inuzuka, B. Dhara, Y. Koyama, K.-I. Nakayama, S. Maeda, F. Araoka and D. Miyajima, *Nature*, 2022, **609**, 502–506.

4 M. Gomberg, *J. Am. Chem. Soc.*, 1900, **22**, 757–771.
5 R. G. Hicks, *Org. Biomol. Chem.*, 2007, **5**, 1321–1338.
6 P. P. Power, *Chem. Rev.*, 2003, **103**, 789–810.
7 H. Fujiwara, E. Ojima and H. Kobayashi, *Synth. Met.*, 2001, **120**, 971–972.
8 A. F. Dobre, C. Lete, V. E. Kuncser, N. Iacob, A. M. Madalan, G. Ionita, M. Harada, Y. Kitagawa and P. Ionita, *ACS Omega*, 2025, **10**, 36662–36671.
9 B. K. Rugg, M. D. Krzyaniak, B. T. Phelan, M. A. Ratner, R. M. Young and M. R. Wasielewski, *Nat. Chem.*, 2019, **11**, 981–986.
10 Y. Joo, V. Agarkar, S. H. Sung, B. M. Savoie and B. W. Boudouris, *Science*, 2018, **359**, 1391–1395.
11 Y. Qu, Y. Li, X. Tan, W. Zhai, G. Han, J. Hou, G. Liu, Y. Song and Y. Liu, *Chem. Eur. J.*, 2019, **25**, 7888–7895.
12 S. Ohira, K. Nakayama, T. Ise, T. Ishida, T. Nogami, I. Watanabe and K. Nagamine, *Polyhedron*, 2001, **20**, 1223–1227.
13 S. A. Green, D. J. Simpson, G. Zhou, P. S. Ho and N. V. Blough, *J. Am. Chem. Soc.*, 1990, **122**, 7337–7346.
14 G. N. Lewis, D. Lipkin and T. T. Magel, *J. Am. Chem. Soc.*, 1944, **66**, 1579–1583.
15 R. Beaulac, D. Luneau and C. Reber, *Chem. Phys. Lett.*, 2005, **405**, 153–158.
16 I. Y. Barskaya, S. L. Veber, E. A. Suturina, P. S. Sherin, K. Y. Maryunina, N. A. Artiukhova, E. V. Tretyakov, R. Z. Sagdeev, V. I. Ovcharenko, N. P. Gritsan and M. V. Fedin, *Dalton Trans.*, 2017, **13**, 101957.
17 E. V. Tretyakov, V. F. Plyusnin, A. O. Suvorova, S. V. Larionov, S. A. Popov, O. V. Antonova, E. M. Zueva, D. V. Stass, A. S. Bogomyakov, G. V. Romanenko and V. I. Ovcharenko, *J. Luminescence*, 2014, **148**, 33–38.
18 H. M. Blatter and H. Lukaszewski, *Tetrahedron Lett.*, 1968, **9**, 2701–2705.
19 G. Karecla, P. Papagiorgis, N. Panagi, G. A. Zissimou, C. P. Constantinides, P. A. Koutentis, G. Itskos and S. C. Hayes, *New J. Chem.*, 2017, **41**, 8604–8613.
20 P. Bartos, B. Anand, A. Pietrzak and P. Kaszyński, *Org. Lett.*, 2019, **22**, 180–184.
21 D. Gulyaev, A. Serykh, E. Tretyakov, A. Akyeva, M. Syroeshkin, D. E. Gorbunov, S. V. Maltseva, N. P. Gritsan, G. Romanenko and A. Bogomyakov, *Catalysts*, 2023, **13**, 1206.
22 P. Bartos, P. Szamweber, B. Camargo, A. Pietrzak and P. Kaszyński, *Chem. Sci.*, 2025, **16**, 12139–12147.
23 M. Ballester, *Pure Appl. Chem.*, 1967, **15**, 123–151.
24 M. A. Fox, E. Gaillard and C. C. Chen, *J. Am. Chem. Soc.*, 1987, **109**(23), 7088–7094.
25 S. R. Ruberu and M. A. Fox, *J. Phys. Chem.*, 1993, **97**, 143–149.
26 A. Heckmann, C. Lambert, M. Goebel and R. Wortmann, *Angew. Chem., Int. Ed.*, 2004, **43**, 5851–5856.
27 A. Heckmann, S. Dümmler, J. Pauli, M. Margraf, J. Köhler, D. Stich, C. Lambert, I. Fischer and U. Resch-Genger, *J. Phys. Chem. C*, 2009, **113**, 20958–20966.
28 H. Guo, Q. Peng, X.-K. Chen, Q. Gu, S. Dong, E. W. Evans, A. J. Gillett, X. Ai, M. Zhang, D. Credgington, V. Coropceanu, R. H. Friend, J.-L. Brédas and F. Li, *Nat. Mater.*, 2019, **18**, 977–984.
29 O. Armet, J. Veciana, C. Rovira, J. Riera, J. Castaner, E. Molins, J. Rius, C. Miravitlles, S. Olivella and J. Brichfeus, *J. Phys. Chem.*, 1987, **91**, 5608–5616.
30 V. Gamero, D. Velasco, S. Latorre, F. López-Calahorra, E. Brillas and L. Juliá, *Tetrahedron Lett.*, 2006, **47**, 2305–2309.
31 Q. Peng, A. Obolda, M. Zhang and F. Li, *Angew. Chem., Int. Ed.*, 2015, **54**, 7091–7095.
32 X. Ai, E. W. Evans, S. Dong, A. J. Gillett, H. Guo, Y. Chen, T. J. H. Hele, R. H. Friend and F. Li, *Nature*, 2018, **563**, 536–540.
33 A. Abdurahman, T. J. H. Hele, Q. Gu, J. Zhang, Q. Peng, M. Zhang, R. H. Friend, F. Li and E. W. Evans, *Nat. Mater.*, 2020, **19**, 1224–1229.
34 J. Ding, M. Zhang, Y. Gao, C. Lu, M. Zhang and F. Li, *J. Phys. Chem. Lett.*, 2023, **14**, 8244–8250.
35 C. Lu, E. Cho, K. Wan, C. Wu, Y. Gao, V. Coropceanu, J. L. Brédas and F. Li, *Adv. Funct. Mater.*, 2024, **34**, 2314811.
36 Y. Xie, S. Wu, Z. Zhu, J. Wang, Z. Kuang, L. Zhang, A. Abdurahman, Q. Peng and X. Ai, *Angew. Chem., Int. Ed.*, 2025, **64**, e202515346.
37 Y. Hattori, T. Kusamoto and H. Nishihara, *Angew. Chem.*, 2014, **126**, 12039–12042.
38 Y. Hattori, T. Kusamoto and H. Nishihara, *RSC Adv.*, 2015, **5**, 64802–64805.
39 A. Abdurahman, Y. Chen, X. Ai, O. Ablikim, Y. Gao, S. Dong, B. Li, B. Yang, M. Zhang and F. Li, *J. Mater. Chem. C*, 2018, **6**, 11248–11254.
40 Y. Hattori, S. Kimura, T. Kusamoto, H. Maeda and H. Nishihara, *Chem. Commun.*, 2018, **54**, 615–618.
41 H. D. Hartzler, *J. Org. Chem.*, 1966, **31**, 2654–2658.
42 H. Suzuki, H. Koide and T. Ogawa, *Bull. Chem. Soc. Japan*, 1988, **61**, 501–504.
43 H. A. P. De Jongh, C. R. H. I. De Jonge, H. J. M. Sinnige, W. J. De Klein, W. G. B. Huysmans, W. J. Mijs, W. J. Van den Hoek and J. Smidt, *J. Org. Chem.*, 1972, **37**, 1960–1966.
44 H. A. P. De Jongh, C. R. H. I. De Jonge and W. J. Mijs, *J. Org. Chem.*, 1971, **36**, 3160–3168.
45 T. Kobashi, D. Sakamaki and S. Seki, *Angew. Chem., Int. Ed.*, 2016, **55**, 8634–8638.
46 J. P. Peterson, M. R. Geraskina, R. Zhang and A. H. Winter, *J. Org. Chem.*, 2017, **82**, 6497–6501.
47 K. Okino, S. Hira, Y. Inoue, D. Sakamaki and S. Seki, *Angew. Chem., Int. Ed.*, 2017, **56**, 16597–16601.
48 R. Zhang, A. Ellern and A. H. Winter, *Angew. Chem., Int. Ed.*, 2021, **60**, 25082–25088.
49 K. Okino, D. Sakamaki and S. Seki, *ACS Mater. Lett.*, 2019, **1**, 25–29.
50 Y. Xu, D. Yin, Y. Wang, D. Chen, X. Li and L. Yan, *Angew. Chem., Int. Ed.*, 2025, **64**, e202509609.
51 L. Li, C. R. Prindle, W. Shi, C. Nuckolls and L. Venkataraman, *J. Am. Chem. Soc.*, 2023, **145**, 18182–18204.
52 K. Yang, X. Zhang, A. Harbuzaru, L. Wang, Y. Wang, C. Koh, H. Guo, Y. Shi, J. Chen, H. Sun, K. Feng, M. C. Ruiz Delgado, H. Y. Woo, R. P. Ortiz and X. Guo, *J. Am. Chem. Soc.*, 2020, **142**, 4329–4340.
53 S. Lukman, J. M. Richter, L. Yang, P. Hu, J. Wu, N. C. Greenham and A. J. Musser, *J. Am. Chem. Soc.*, 2017, **139**, 18376–18385.
54 Y. Zhu, Z. Zhu, S. Wang, Q. Peng and A. Abdurahman, *Angew. Chem., Int. Ed.*, 2025, **64**, e202423470.
55 X. Hu, H. Chen, L. Zhao, M. Miao, J. Han, J. Wang, J. Guo, Y. Hu and Y. Zheng, *Chem. Commun.*, 2019, **55**, 7812–7815.
56 T. Kubo, *Pure Appl. Chem.*, 2023, **95**, 363–375.
57 Y. Ni and J. Wu, *Tetrahedron Lett.*, 2016, **57**, 5426–5434.
58 Y. Hattori, K. Yamamoto, R. Kitajima and K. Uchida, *Chemistry*, 2024, **30**, e202304124.
59 Z. Zhou, K. Yang, L. He, W. Wang, W. Lai, Y. Yang, Y. Dong, S. Xie, L. Yuan and Z. Zeng, *J. Am. Chem. Soc.*, 2024, **146**, 6763–6772.
60 X. Chang, M. E. Arnold, R. Blinder, J. Zolg, J. Wischnat, J. van Slageren, F. Jelezko, A. J. C. Kuehne and M. von Delius, *Angew. Chem., Int. Ed.*, 2024, **63**, e202404853.
61 C.-H. Liu, Z. He, C. Ruchlin, Y. Che, K. Somers and D. F. Perepichka, *J. Am. Chem. Soc.*, 2023, **145**, 15702–15707.
62 A. Punzi, Y. Dai, C. N. Dibenedetto, E. Mesto, E. Schingaro, T. Ullrich, M. Striccoli, D. M. Guldi, F. Negri, G. M. Farinola and D. Blasi, *J. Am. Chem. Soc.*, 2023, **145**, 20229–20241.
63 C. P. Yu, R. Chowdhury, Y. Fu, P. Ghosh, W. Zeng, T. B. E. Mustafa, J. Grüne, L. E. Walker, D. G. Congrave, X. W. Chua, P. Murto, A. Rao, H. Sirringhaus, F. Plasser, C. P. Grey, R. H. Friend and H. Bronstein, *Sci. Adv.*, 2024, **10**, eado3476.
64 L. Feng, Y. Tuo, Z. Wu, W. Zhang, C. Li, B. Yang, L. Liu, J. Gong, G. Jiang, W. Hu, B. Z. Tang, L. Wu and J. Wang, *J. Am. Chem. Soc.*, 2024, **146**, 32582–32594.
65 M. Abe, *Chem. Rev.*, 2013, **113**, 7011–7088.
66 A. Abdurahman, L. Shen, J. Wang, M. Niu, P. Li, Q. Peng, J. Wang and G. Lu, *Light: Sci. Appl.*, 2023, **12**, 272.
67 S. Wang, X. Wang, J. Ding, Z. Zhu, J. Wang, L. Shen, A. Abdurahman, G. Lu, J. Wang and Q. Peng, *Macromolecules*, 2024, **57**, 6133–6139.
68 Y. Hattori, E. Michail, A. Schmiedel, M. Moos, M. Holzapfel, I. Krummenacher, H. Braunschweig, U. Müller, J. Pflaum and C. Lambert, *Chemistry*, 2019, **25**, 15463–15471.
69 R. Matsuoka, S. Kimura, T. Miura, T. Ikoma and T. Kusamoto, *J. Am. Chem. Soc.*, 2023, **145**, 13615–13622.
70 A. Mizuno, R. Matsuoka, S. Kimura, K. Ochiai and T. Kusamoto, *J. Am. Chem. Soc.*, 2024, **146**, 18470–18483.
71 P. S. Roy and B. J. Saikia, *Indian J. Cancer*, 2017, **53**, 441–442.
72 J. Chen, C. Ning, Z. Zhou, P. Yu, Y. Zhu, G. Tan and C. Mao, *Prog. Mater. Sci.*, 2019, **99**, 1–26.
73 P. Rundle, *Biomedicines*, 2017, **5**, 69.
74 M. Arruebo, N. Vilaboa, B. Sáez-Gutierrez, J. Lambea, A. Tres, M. Valladares and Á. González-Fernández, *Cancers*, 2011, **3**, 3279–3330.

75 X. Bai, W. Tan, A. Abdurahman, X. Li and F. Li, *Dyes Pigments*, 2022, **202**, 110260.
76 X. Li, W. Tan, X. Bai and F. Li, *Chem. Res. Chin. Univ.*, 2023, **39**, 192–196.
77 M. E. Arnold, L. Schoeneburg, M. Lamla and A. J. C. Kuehne, *Molecules*, 2024, **29**, 995.
78 X. Cui, G. Lu, S. Dong, S. Li, Y. Xiao, J. Zhang, Y. Liu, X. Meng, F. Li and C.-S. Lee, *Mater. Horiz.*, 2021, **8**, 571–576.
79 X. Wang, G. Shi, R. Wei, M. Li, Q. Zhang, T. Zhang, C.-F. Chen and H.-Y. Hu, *Chem. Sci.*, 2024, **15**, 6421–6431.
80 Z. Li, Z. Dang, J. Ding, X. Li, S. Zhu and F. Li, *Sens. Actuators, B*, 2024, **414**, 135931.
81 X. Cui, F. Fang, H. Chen, C. Cao, Y. Xiao, S. Tian, J. Zhang, S. Li and C.-S. Lee, *Mater. Horiz.*, 2025, **12**, 1002–1007.
82 D. Chen, Y. Xu, Y. Wang, X. Li, D. Yin and L. Yan, *ACS Appl. Mater. Interfaces*, 2024, **16**, 59907–59920.
83 Y. Xu, C. Teng, H. Dang, D. Yin and L. Yan, *Talanta*, 2024, **266**, 124948.
84 Y. Xu, C. Teng, Y. Wang, D. Chen, D. Yin and L. Yan, *J. Colloid Interface Sci.*, 2024, **669**, 578–589.
85 T. Liu, Z. Zhu, S. Wang, L. Shen, A. Abdurahman, X. Liu and G. Lu, *Light: Sci. Appl.*, 2025, **14**, 289.
86 T. Huang, K. Yang, W. Hu, L. Feng, Z. Wu, H. Chen, J. Wang and Z. Zeng, *Chem*, 2025, **11**, 102621.
87 Q. Zhao, C. Wu, Y. Gao, J. Long, W. Zhang, Y. Chen, Y. Yang, Y. Luo, Y. Lai, H. Zhang, X. Chen, F. Li and S. Li, *Adv. Sci.*, 2025, **12**, 2411733.

